Nucl. Phys. B 1020 (2025) 117147

Contents lists available at ScienceDirect

Nuclear Physics, Section B

journal homepage: www.elsevier.com/locate/nuclphysb

Superradiance, geodesics and shadows of black holes in dark photon with higher-order correction

Shahid Chaudhary [a,b], Muhammad Danish Sultan [c], Talha Anwar [d,e,*], Atif Mossad Ali [f], Farruh Atamurotov [g,h,i], Muhammad Hadi [f], M. A. Sayed [f], Ali M. Mubaraki [j]

[a] Department of Natural Sciences and Humanities, University of Engineering and Technology Lahore, New Campus, Pakistan
[b] Research Center of Astrophysics and Cosmology, Khazar University, 41 Mehseti Street, AZ1096, Baku, Azerbaijan
[c] Department of Physics, Durham University, UK
[d] School of Science, Walailak University, Nakhon Si Thammarat, 80160, Thailand
[e] Research Center for Theoretical Simulation and Applied Research in Bioscience and Sensing, Walailak University, Nakhon Si Thammarat, 80160, Thailand
[f] Department of Physics, Faculty of Science, King Khalid University, Abha, Saudi Arabia
[g] Kimyo International University in Tashkent, Shota Rustaveli str. 156, Tashkent, 100121, Uzbekistan
[h] University of Tashkent for Applied Sciences, Str. Gavhar 1, Tashkent, 100149, Uzbekistan
[i] Tashkent State Technical University, Tashkent, 100095, Uzbekistan
[j] Department of Mathematics and Statistics, College of Science, Taif University, P.O. Box 11099, Taif, 21944, Saudi Arabia

ARTICLE INFO

Editor: Yasaman Farzan

Keywords:
Dark photons
Shadow images
Superradiance
Angular momentum
Orbital velocity

ABSTRACT

The exploration of black holes in the presence of dark photon fields offers a compelling pathway to investigate hidden sector interactions and their gravitational impacts. We analyze static, spherically symmetric black hole solutions within dark photon models featuring Yukawa-type interactions and higher-order magnetic dipole corrections. These modifications are introduced via a generalized energy-momentum tensor sourced by the dark photon field, resulting in a nontrivial deformation of the spacetime geometry. We investigate the dynamics of massless and massive particles, emphasizing the influence of dark sector parameters on effective potentials, photon spheres, and circular geodesics. Notably, the innermost stable circular orbit radius, particle energy, and angular momentum exhibit sensitive dependence on $m_{A'}$ and g_D, suggesting observable deviations in accretion disk behavior and gravitational wave emissions. Through numerical analysis, we compute the shadow radius R_s and demonstrate that dark photon corrections either compress or enlarge the black hole shadow, depending on the interplay between Yukawa screening and gauge coupling. The geodetic precession frequency Θ_{GPF} is also shown to vary significantly from classical expectations, pointing to dark-sector-induced frame-dragging effects. Additionally, we explore the superradiance phenomenon by solving the Klein-Gordon equation for charged scalar perturbations in the modified background. Our results identify conditions for wave amplification and highlight how dark photon interactions can enhance or suppress the superradiant scattering regime. Overall, this study presents a unified framework that connects dark photon physics with black hole thermodynamics, geodesic motion, optical properties, and stability.

* Corresponding author.
E-mail address: anwartalha80@gmail.com (T. Anwar).

https://doi.org/10.1016/j.nuclphysb.2025.117147
Received 16 July 2025; Received in revised form 11 September 2025; Accepted 26 September 2025
Available online 2 October 2025

1. Introduction

The study of black holes (BHs) remains a central theme in theoretical physics, with implications for quantum gravity, astrophysics, and cosmology. In recent years, the exploration of modified gravity theories and beyond-Standard-Model physics has led to the incorporation of additional fields and interactions into the structure of BHs. One such intriguing proposal involves the inclusion of dark photons, which arise from a hidden U(1) gauge symmetry associated with the dark matter sector [1–3]. These fields can interact with standard matter either through kinetic mixing or higher-order operators, resulting in novel corrections to the gravitational field equations. In this context, studying solutions within dark photon model (DPM) provides a promising avenue for probing the imprints of dark sector physics on gravitational systems. In particular, dark photons can give rise to Yukawa-type corrections and magnetic dipole-type interactions that modify the spacetime geometry near compact objects. These higher-order corrections become especially significant in strong-field regimes, such as the vicinity of BHs. The resulting modifications to the metric function affect not only the BH's horizon structure and thermodynamics but also the motion of test particles, optical characteristics like shadows, and dynamical processes such as superradiance. Previous investigations into BHs with nonminimal couplings and hidden sector fields have revealed a wide range of physical effects [4–6].

The dynamics of massless and massive particles in curved spacetimes is a powerful tool for understanding the geometry of a given BH solution. Geodesic motion provides insight into observational phenomena such as lensing, time delay, and the structure of accretion disks. In the presence of dark photon corrections, the effective potential governing particle motion is significantly altered, leading to deviations from Schwarzschild or RN-like trajectories. Studies of null geodesics in modified gravity theories [7–9] have shown that additional fields can shift the location of photon spheres, alter the stability of circular orbits, and affect observable quantities such as the innermost stable circular orbit (ISCO) and Lyapunov exponents. One of the most prominent observational features of BHs is their shadow, which arises due to the capture of light by the photon sphere and serves as a silhouette against a backdrop of luminous matter. The recent observations by the Event Horizon Telescope have provided the first direct images of BH shadows [10], inspiring numerous theoretical models that incorporate deviations from general relativity. In this vein, the impact of dark photons on the shadow is a subject of considerable interest, as modifications to the lapse function can lead to measurable changes in the shadow radius and its deformation [11–13]. The shadow's size, shape, and distortion are directly linked to the underlying spacetime geometry and can be used to constrain the parameter space of dark sector models.

Another fascinating phenomenon that connects quantum field theory with general relativity is the process of superradiance. This refers to the amplification of waves scattered off a rotating or charged , provided the frequency of the incident wave lies within a specific regime [14,15]. The existence of light bosonic fields, such as dark photons, can trigger superradiant instabilities, potentially leading to the formation of gravitational atoms or affecting the spin evolution of BHs. Studies have shown that the coupling between scalar or vector fields and spacetimes can significantly enhance superradiant amplification [16,17]. In our case, the inclusion of higher-order corrections in the DPM modifies the effective potential for scalar perturbations and changes the conditions for wave amplification.

Despite the remarkable success of general relativity in describing gravitational phenomena, the nature of dark matter and its interaction with gravity remains one of the most profound unresolved problems in modern physics. Among various candidates proposed to mediate interactions within the dark sector, dark photons gauge bosons associated with a hidden U(1) symmetry have emerged as promising extensions of the Standard Model. These fields can couple to ordinary matter through kinetic mixing or higher-order operators and are capable of inducing nontrivial modifications to the spacetime geometry around compact objects. The BHs, being natural laboratories for extreme gravitational environments, offer an ideal platform to investigate such hidden sector effects. The incorporation of dark photon-induced corrections specifically Yukawa type and magnetic dipole interactions into metrics not only enriches our theoretical understanding of modified gravity but also yields potentially observable signatures, such as changes in horizon structure, orbital dynamics, shadow deformation, and superradiant scattering. This study is motivated by the need to bridge the gap between gravitational theory and dark sector physics by exploring how dark photons imprint themselves on thermodynamics, particle motion, and optical features. By constructing and analyzing BH solutions within this framework, we aim to provide new insights into the interplay between dark matter interactions and strong-field gravity, with implications for both fundamental theory and astrophysical observations.

The paper is organized as follows. In Section II, we provide static, spherically symmetric solutions in DPM with higher-order corrections and analyze the modified metric function. Section III investigates the dynamics of massless and massive particles by examining the effective potential, circular orbits, and stability conditions. In Section IV, we study the optical appearance of the BH, including the photon sphere and shadow radius, highlighting the effects of dark photon parameters. Section V is devoted to the phenomenon of superradiance, where we solve the charged Klein-Gordon equation in the modified geometry and identify conditions for wave amplification. Finally, we conclude with a summary of the key findings and their physical implications in the concluding section.

2. Black hole solutions in dark photon models with higher order corrections

The exploration of solutions in the presence of dark photon fields provides a framework to understand potential interactions between dark matter and gravity. Dark photons arises from a $U(1)$ gauge symmetry, offer a natural extension to the standard model of particle physics and introduce nontrivial corrections to the classical Einstein field equations. In this section, we consider a static, spherically symmetric solution that incorporates both minimal (Yukawa-type) and higher-order magnetic dipole interactions associated with the dark photon field. These interactions yield a modified metric function $f(r)$ that encapsulates the energy-momentum

contributions from the dark sector. By analyzing the resulting spacetime geometry, we aim to elucidate the physical implications of such corrections, particularly their influence on the BH's horizon structure, energy density, and thermodynamic properties. This analysis sets the foundation for examining the dynamical and observational features of these modified configurations in subsequent sections. We start by considering static, spherically symmetric BH solution

$$ds^2 = -f(r)\,dt^2 + \frac{dr^2}{f(r)} + r^2\left(d\theta^2 + \sin^2\theta\,d\phi^2\right), \tag{1}$$

where $f(r)$ is metric function captures the gravitational modifications arising from the dark photon sector. The effective energy density contributed by the dark photon can be obtained from the Laplacian of the potential corrections, as shown in [18,19]

$$\rho(r) = \frac{1}{4\pi}\,\Delta V(r), \tag{2}$$

Consequently, the full effective potential is given by [20]

$$V(r) = V_{\min}(r) + V_{\mathrm{MD}}(r), \tag{3}$$

where we include both minimal (Yukawa) and magnetic dipole contributions. The corresponding potentials are expressed as

$$V_{\min}(r) = -\frac{g_D^2}{4\pi}\frac{e^{-m_{A'}r}}{r}, \tag{4}$$

and

$$V_{\mathrm{MD}}(r) \approx -\frac{\mu_f^2}{\Lambda^2}\frac{1}{4\pi}\frac{e^{-m_{A'}r}}{r^3}\left[\boldsymbol{\sigma}_1\cdot\boldsymbol{\sigma}_2 - 3(\boldsymbol{\sigma}_1\cdot\hat{\mathbf{r}})(\boldsymbol{\sigma}_2\cdot\hat{\mathbf{r}})\right] \equiv -\frac{\mu_f^2}{\Lambda^2}\frac{1}{4\pi}\frac{e^{-m_{A'}r}}{r^3}S_{12}. \tag{5}$$

where the negative sign in the potential terms suggests possible violations of classical energy conditions near the BH. The coupling constant g_D quantifies the strength of interaction between dark matter and the dark photon field [21]. The quantity $m_{A'}$ represents the mass of the dark photon, a gauge boson associated with a hidden $U(1)$ symmetry. The symbol μ_f stands for the magnetic dipole moment of the dark matter fermion, while Λ is the energy scale at which higher-dimensional operators from new physics become relevant. The term S_{12} is the spin-tensor interaction factor, defined as $S_{12} = [\boldsymbol{\sigma}_1\cdot\boldsymbol{\sigma}_2 - 3(\boldsymbol{\sigma}_1\cdot\hat{r})(\boldsymbol{\sigma}_2\cdot\hat{r})]$, which encodes spin-spin couplings between fermionic dark matter particles. Finally, r is the radial coordinate measuring the distance from the center. We compute the corresponding Laplacians as detailed in [20]

$$\Delta V_{\min}(r) = -\frac{g_D^2 m_{A'}^2}{4\pi}\frac{e^{-m_{A'}r}}{r} + g_D^2\,\delta^{(3)}(\vec{r}), \tag{6}$$

$$\Delta V_{\mathrm{MD}}(r) \approx -\frac{\mu_f^2}{\Lambda^2}\frac{1}{4\pi}e^{-m_{A'}r}\left(\frac{m_{A'}^2}{r^3} + \frac{4m_{A'}}{r^4} + \frac{6}{r^5}\right)S_{12}. \tag{7}$$

Ignoring delta-function terms for $r > 0$, the energy density is given by [20]

$$\rho(r) = -\frac{g_D^2 m_{A'}^2}{(4\pi)^2}\frac{e^{-m_{A'}r}}{r} - \frac{\mu_f^2 S_{12}}{\Lambda^2(4\pi)^2}e^{-m_{A'}r}\left(\frac{m_{A'}^2}{r^3} + \frac{4m_{A'}}{r^4} + \frac{6}{r^5}\right). \tag{8}$$

Therefore, the modified Einstein equation for the tt-component takes the form

$$\frac{rf'(r) + f(r) - 1}{r^2} = -8\pi\rho(r), \tag{9}$$

which results in

$$\frac{d}{dr}\left[rf(r)\right] = 1 + \frac{g_D^2 m_{A'}^2}{2\pi}re^{-m_{A'}r} + \frac{\mu_f^2 S_{12}}{2\pi\Lambda^2}e^{-m_{A'}r}\left(\frac{m_{A'}^2 r}{1} + \frac{4m_{A'}}{1} + \frac{6}{r}\right). \tag{10}$$

By integrating and choosing the integration constant $C = -2M$ to ensure the Schwarzschild behavior is recovered at large r, we arrive at

$$f(r) = 1 - \frac{2M}{r} - \frac{g_D^2 m_{A'}}{2\pi}\frac{e^{-m_{A'}r}}{1} - \frac{g_D^2}{2\pi}\frac{e^{-m_{A'}r}}{r} + \frac{\mu_f^2 S_{12}}{2\pi\Lambda^2}\frac{I(r)}{r}, \tag{11}$$

where

$$I(r) = -2m_{A'}^2\,\mathrm{Ei}(-m_{A'}r) - \frac{m_{A'}e^{-m_{A'}r}}{r} - \frac{3e^{-m_{A'}r}}{r^2}, \tag{12}$$

where $\mathrm{Ei}(z)$ denotes the exponential integral function. Under the weak-field approximation, the metric function simplifies to more manageable analytical expressions in two limiting cases:

1. **Small-distance limit** ($m_{A'}r \ll 1$):
   At short distances, using the approximations $e^{-m_{A'}r} \approx 1$ and $\mathrm{Ei}(-m_{A'}r) \approx \gamma + \ln(m_{A'}r)$, one obtains

$$f(r) \approx 1 - \frac{2M}{r} + \frac{g_D^2}{2\pi r}(m_{A'}r + 1) + \frac{\mu_f^2 S_{12}}{2\pi\Lambda^2}\left[\frac{2m_{A'}^2(\gamma + \ln(m_{A'}r))}{r} + \frac{m_{A'}}{r^2} + \frac{3}{r^3}\right], \tag{13}$$

   where $\gamma \approx 0.5772$ is the Euler-Mascheroni constant.
2. **Large-distance limit** ($m_{A'}r \gg 1$):
   At large distances, one finds $\mathrm{Ei}(-m_{A'}r) \approx -\frac{e^{-m_{A'}r}}{m_{A'}r}$, yielding [20]

$$f(r) \approx 1 - \frac{2M}{r} + \frac{g_D^2}{2\pi}\frac{e^{-m_{A'}r}(m_{A'}r + 1)}{r} - \frac{\mu_f^2 S_{12} m_{A'} e^{-m_{A'}r}}{2\pi\Lambda^2 r^2}. \tag{14}$$

where parameter M denotes the mass of the in geometric units ($G = c = 1$). Physically, the Yukawa-type correction (second term) dominates at intermediate distances ($r \sim 1/m_{A'}$), whereas the magnetic dipole correction (third term) becomes significant at shorter distances due to its faster decay with r. As $r \to \infty$, both correction terms vanish, and the spacetime asymptotically approaches the standard Schwarzschild geometry. The mass of BH solutions in DPMs is not a fixed parameter but is influenced by the interactions between the BH and dark photons. These interactions can modify the spacetime geometry near the BH, leading to changes in observable quantities such as the horizon radius and Hawking temperature. The event horizon $r = r_+$ of the metric given in Eq. (14) is defined by the condition $f(r_+) = 0$. At large distances, this horizon condition determines the mass as follows

$$M = \frac{r_+}{2}\left[1 + \frac{g_D^2}{2\pi}\frac{e^{-m_{A'}r_+}(m_{A'}r_+ + 1)}{r_+} - \frac{\mu_f^2 S_{12} m_{A'} e^{-m_{A'}r_+}}{2\pi\Lambda^2 r_+^2}\right]. \tag{15}$$

In DPM, the Hawking temperature of BH solutions can be modified by the presence of dark photons, which are particles associated with DM. Dark photons can couple to standard electromagnetic fields or directly affect the spacetime geometry around BHs, which in turn influences their thermodynamic properties, including their Hawking temperature. The Hawking temperature, defined via the surface gravity $\kappa = \frac{f'(r_+)}{2}$, becomes

$$T_H = \frac{f'(r_+)}{4\pi}, \tag{16}$$

with

$$f'(r_+) = \frac{2M}{r_+^2} - \frac{g_D^2}{2\pi}\left[m_{A'}^2 e^{-m_{A'}r_+} + \frac{e^{-m_{A'}r_+}(m_{A'}r_+ + 1)}{r_+^2}\right] + \frac{\mu_f^2 S_{12}}{2\pi\Lambda^2}\left[\frac{m_{A'}e^{-m_{A'}r_+}}{r_+^2} + \frac{2e^{-m_{A'}r_+}}{r_+^3}\right]. \tag{17}$$

These expressions clearly illustrate the physical impact of dark photon corrections, showing changes in both the horizon radii and the temperature.

Having established the modified BH solutions in the presence of dark photon fields with Yukawa-type and higher-order magnetic dipole corrections, it is natural to explore how these deformations influence the motion of test particles in the resulting spacetime. Since geodesic motion serves as a fundamental probe of the underlying geometry, analyzing the trajectories of both massless and massive particles provides direct insights into the physical implications of dark photon corrections. In particular, studying circular orbits, stability conditions, and critical radii such as the photon sphere and ISCO allow us to connect the abstract modifications of the metric to observable astrophysical phenomena, including accretion disk dynamics, precession effects, and potential gravitational wave signatures.

3. Geodesic motion of test particles around black hole in dark photon models

3.1. Null geodesics and photon spheres

Understanding the motion of test particles around BHs provides information about the geometry of spacetime and the effects of additional fields or interactions. In the context of DPMs, the presence of vector fields coupled to gravity significantly alters the geodesic structure, thereby influencing both massless (photons) and massive particle trajectories. This section is devoted to investigating the dynamical behavior of particles in the vicinity of a spherically symmetric solution modified by dark photon corrections. By analyzing the effective potential, we examine how the dark gauge coupling g_D and dark photon mass $m_{A'}$ affect the stability of orbits, the structure of photon spheres, and the characteristic features of circular motion. Given that the spacetime is static and spherically symmetric, the analysis of geodesic motion can be confined, without loss of generality, to the equatorial plane by setting $\theta = \pi/2$ and $\dot{\theta} = 0$. Using the metric tensor $g_{\mu\nu}$, the corresponding Lagrangian density is given by [22]

$$\mathcal{L} = \frac{1}{2} g_{\mu\nu}\dot{x}^\mu \dot{x}^\nu,$$

here, the dot represents differentiation with respect to the affine paramete τ. With the metric given by (1), the Lagrangian density takes the explicit form

$$\mathcal{L} = \frac{1}{2}\left(-f(r)\dot{t}^2 + \frac{\dot{r}^2}{f(r)} + r^2\dot{\phi}^2\right). \tag{18}$$

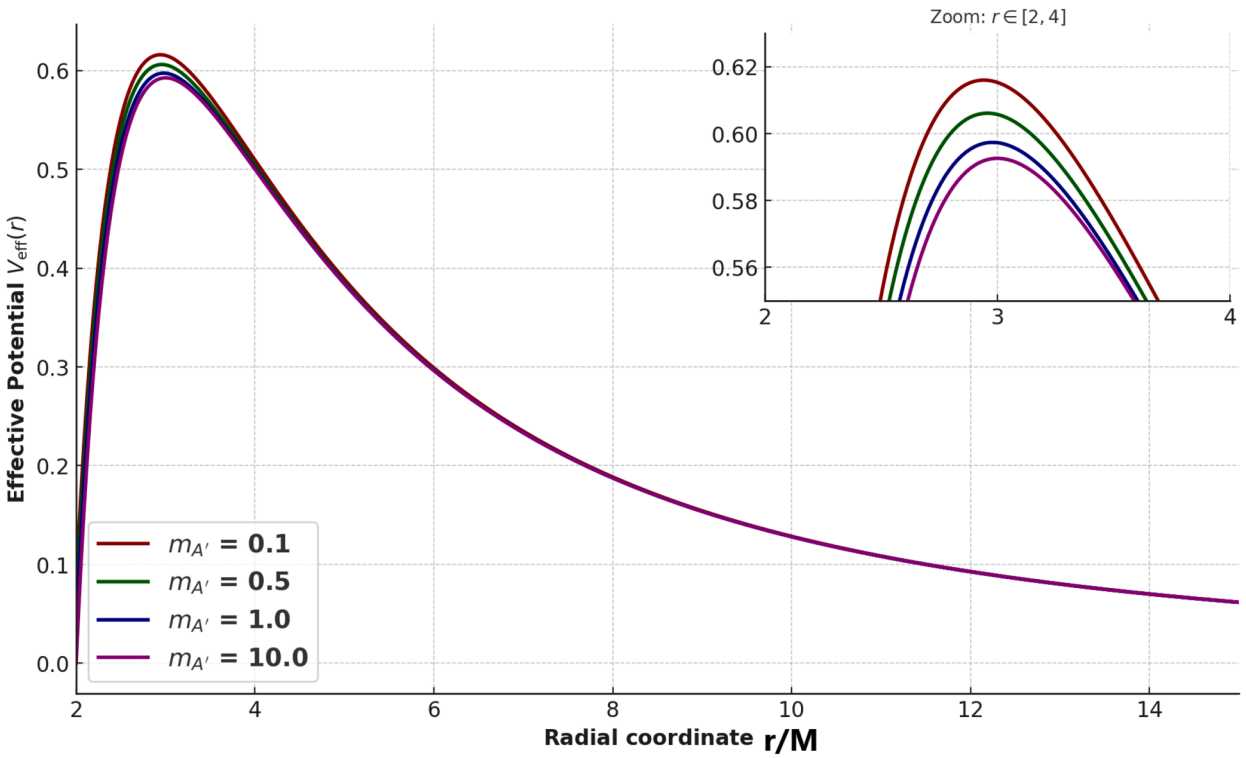

Fig. 1. The plot of effective potential $V_{\text{eff}}(r)$ for null geodesics as a function of radial coordinate r/M for BH solutions in DPM for different values of $m_{A'}M$ for fixed $M = g_D = 0.5$, $\mu_f = S_{12} = 1$ and $\Lambda = 1.7$.

The metric tensor $g_{\mu\nu}$ in the line element (1) is independent of the coordinates (t, ϕ), giving rise to two Killing vectors $\xi^{(t)}$ and $\xi^{(\phi)}$. As a result, two quantities are conserved the energy E and the angular momentum L,which are expressed as follows

$$E = f(r)\dot{t}, \tag{19}$$

$$L = r^2\dot{\phi}. \tag{20}$$

Utilizing these quantities, we obtain the geodesic equation for the radial coordinate r as

$$\dot{r}^2 + V_{\text{eff}}(r) = E^2, \tag{21}$$

here effective potential $V_{\text{eff}}(r)$ for null ($\kappa = 0$) or timelike ($\kappa = -1$) geodesics is given by

$$V_{\text{eff}}(r) = \left(-\kappa + \frac{L^2}{r^2}\right)\left[1 - \frac{2M}{r} + \frac{g_D^2}{2\pi r}e^{-m_{A'}r}(m_{A'}r + 1) - \frac{\mu_f^2 S_{12} m_{A'} e^{-m_{A'}r}}{2\pi\Lambda^2 r^2}\right]. \tag{22}$$

Eq. (22) clearly demonstrates that parameters such as the dark gauge coupling g_D and the dark photon mass $m_{A'}$, play a significant role in shaping the effective potential, thereby affecting the dynamics of the particle. Now, we investigate the optical properties associated with the BH metric, focusing on the influence of the dark gauge coupling g_D and the dark photon mass $m_{A'}$. For null geodesics, where $\kappa = 0$, the effective potential from Eq. (22) reduces to [22]

$$V_{\text{eff}}(r) = \left(\frac{L^2}{r^2}\right)\left[1 - \frac{2M}{r} + \frac{g_D^2}{2\pi r}e^{-m_{A'}r}(m_{A'}r + 1) - \frac{\mu_f^2 S_{12} m_{A'} e^{-m_{A'}r}}{2\pi\Lambda^2 r^2}\right]. \tag{23}$$

This formula describes how light rays move through spacetime and plays a key role in understanding optical effects such as photon spheres, gravitational lensing, and the shadows cast by BHs. The dark gauge coupling g_D and the dark photon mass $m_{A'}$ significantly alters the typical dynamics associated with Schwarzschild or RN-like spacetimes.

Figs. 1 to 3 illustrate the behavior of the effective potential $V_{\text{eff}}(r)$ for null geodesics in the spacetime of solutions influenced by DPM, emphasizing the roles of the dark photon mass $m_{A'}$ and the dark gauge coupling g_D. In Fig. 1, the effective potential is plotted for varying values of $m_{A'}$ while keeping g_D fixed. It is evident that an increase in $m_{A'}$ leads to a decrease in the peak height of $V_{\text{eff}}(r)$ and a slight shift of the potential maximum towards smaller radial distances. This behavior indicates that heavier dark photons cause the photon sphere to shrink and reduce the barrier potential experienced by null particles. Fig. 2 explores the impact of varying g_D for a fixed dark photon mass. As g_D increases, the height of the effective potential increases and shifts outward, indicating that stronger coupling enhances the gravitational lensing region and increases the stability range of photon orbits. Fig. 3 provides a

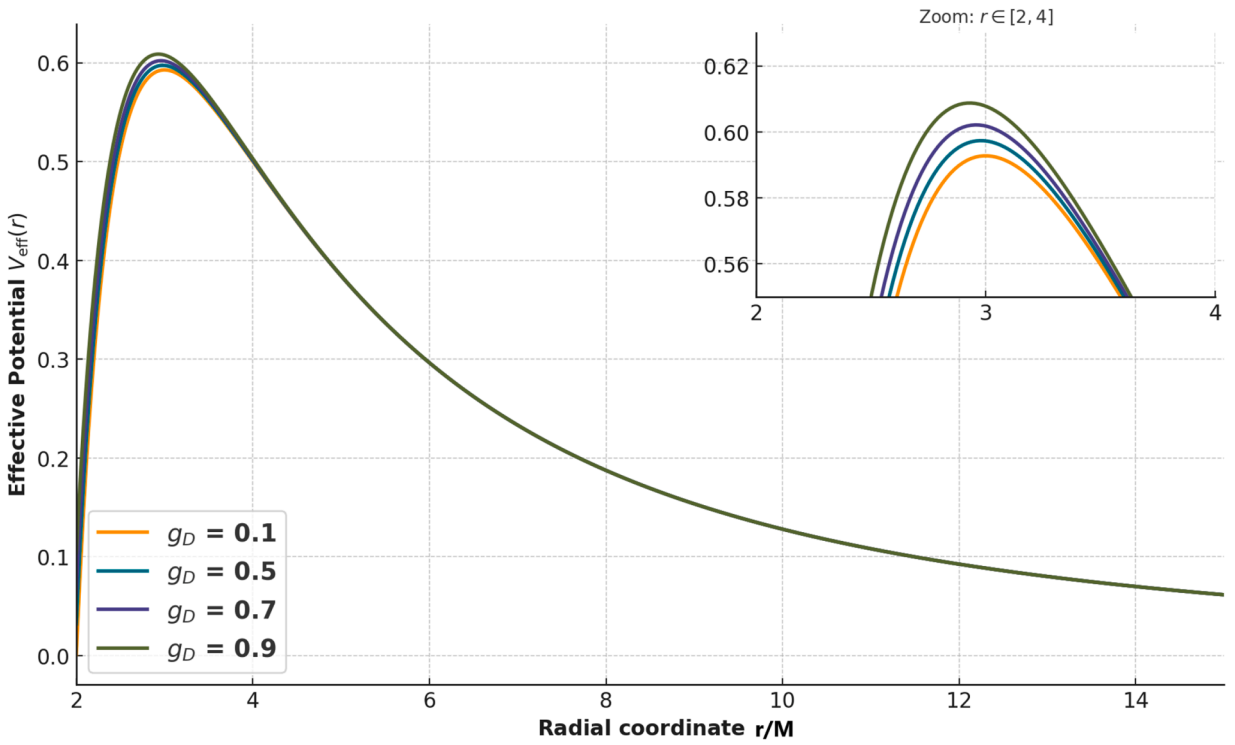

Fig. 2. The plot of effective potential $V_{\text{eff}}(r)$ for null geodesics as a function of radial coordinate r/M for BH solutions in DPM for different values of g_D for fixed, $M = m_{A'}M = 0.5$, $\mu_f = S_{12} = 1$ and $\Lambda = 1.7$.

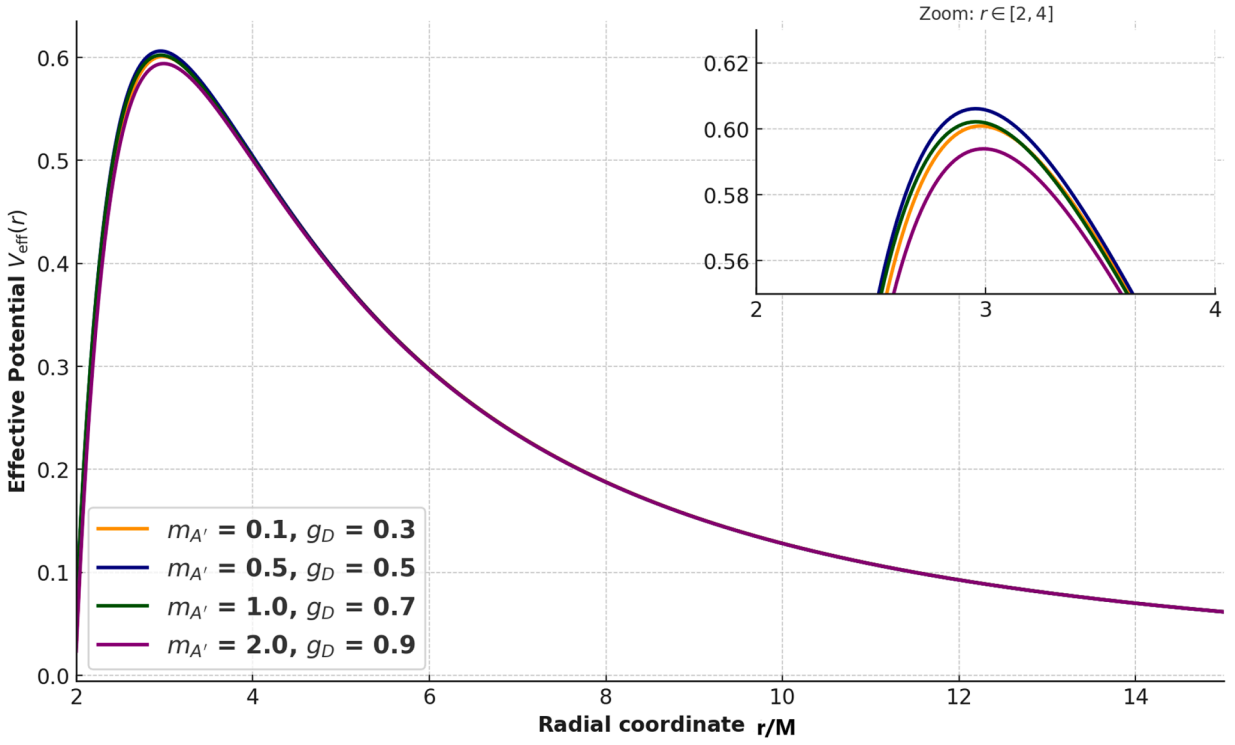

Fig. 3. The plot of effective potential $V_{\text{eff}}(r)$ for null geodesics as a function of radial coordinate r/M for BH solutions in DPM for different values of $m_{A'}M$ and g_D for fixed $M = 0.5$, $\mu_f = S_{12} = 1$ and $\Lambda = 1.7$.

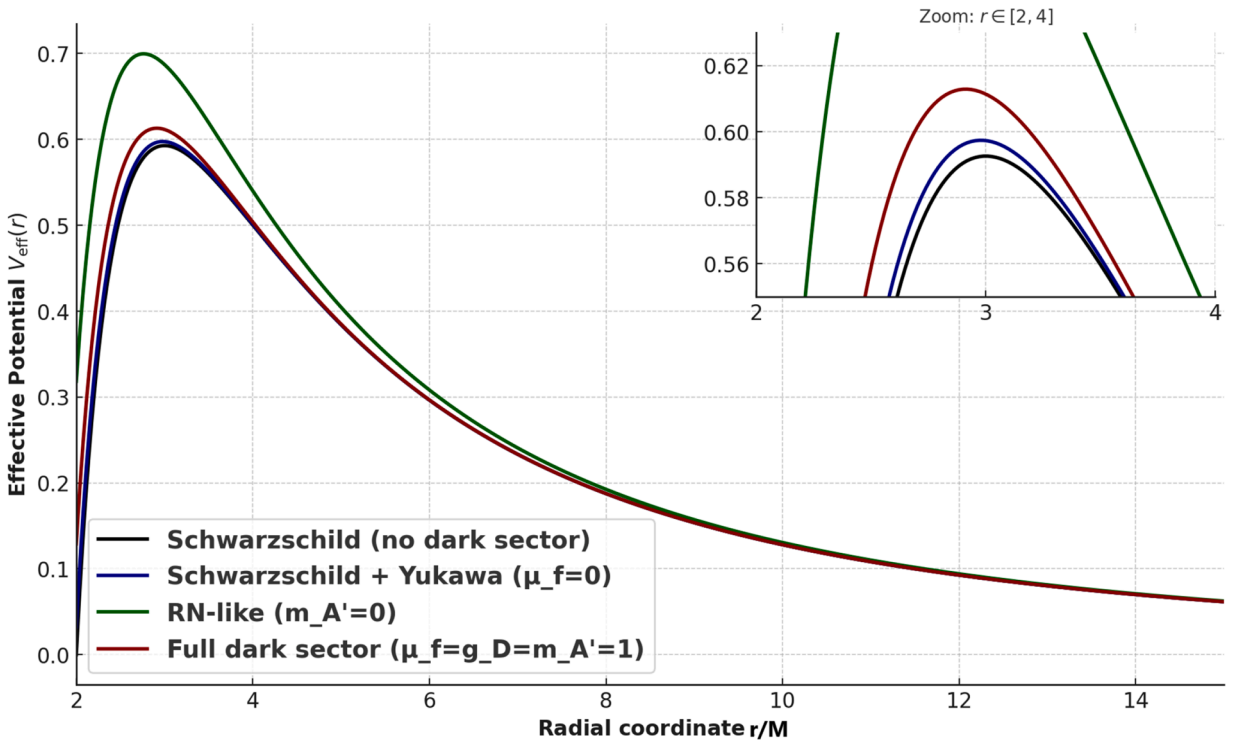

Fig. 4. The plot of effective potential $V_{\text{eff}}(r)$ for null geodesics as a function of radial coordinate r/M for BH solutions in DPM, Schwarzschlid and RN-like BHs.

combined visualization of the interplay between $m_{A'}$ and g_D, revealing the competing effects of the two parameters: while $m_{A'}$ tends to compress the photon orbit region inward, g_D counteracts this by stretching the potential outward. These findings demonstrate that the dark photon parameters significantly alter the geodesic structure and hence the photon capture cross-section and gravitational lensing characteristics of the . Physically, such modifications imply that the presence of dark photon fields deforms the spacetime geometry near the , which can manifest as observable deviations in the shape and size of shadows or the trajectories of null particles. This underscores the importance of incorporating dark sector corrections in gravitational modeling and offers a potential avenue for constraining dark photon properties through observational astrophysics.

Fig. 4 presents a comparative analysis of the effective potential $V_{\text{eff}}(r)$ for null geodesics in spacetimes within DPM, with those from classical Schwarzschild and RN-like BHs. This comparison highlights the distinctive modifications introduced by the inclusion of Yukawa-type and magnetic dipole corrections stemming from the dark photon sector. The effective potential in DPM exhibits a steeper and broader potential barrier compared to the Schwarzschild case, indicating that light rays encounter a stronger repulsive effect near the photon sphere. Relative to the RN-like BH, the dark photon potential shows a more significant shift in the location and height of the potential peak, driven by the additional spin-dependent dipole contributions and exponential suppression terms in the metric function $f(r)$. These corrections modify the geodesic structure and photon capture zone by either enhancing or reducing the stability of photon orbits, depending on the parameter choices for g_D and $m_{A'}$. The key physical implication is that dark photon interactions introduce nontrivial energy-momentum components which deform the spacetime geometry more dynamically than classical charge effects in RN-like geometry. As a result, the observable photon ring and the shape of the shadow could substantially differ from standard general relativity predictions.

For circular null geodesics, the conditions $\dot{r} = 0$ and $\ddot{r} = 0$ must be satisfied, leading to the following relations

$$V_{\text{eff}}(r) = E^2, \quad V'_{\text{eff}}(r) = 0. \tag{24}$$

From the first relation, we obtain the critical impact parameter β_c for a photon ray, defined by

$$\frac{1}{\beta_c} = \frac{E}{L} = \frac{1}{r_c}\left(1 - \frac{2M}{r_c} + \frac{g_D^2}{2\pi r_c} e^{-m_{A'} r_c}(m_{A'} r_c + 1) - \frac{\mu_f^2 S_{12} m_{A'} e^{-m_{A'} r_c}}{2\pi \Lambda^2 {r_c}^2}\right)^{1/2}, \tag{25}$$

here r_c represents the radius of the circular photon orbit. The second condition defines the photon sphere radius, which is given by the following equation

$$2f(r_c) = r_c f'(r_c). \tag{26}$$

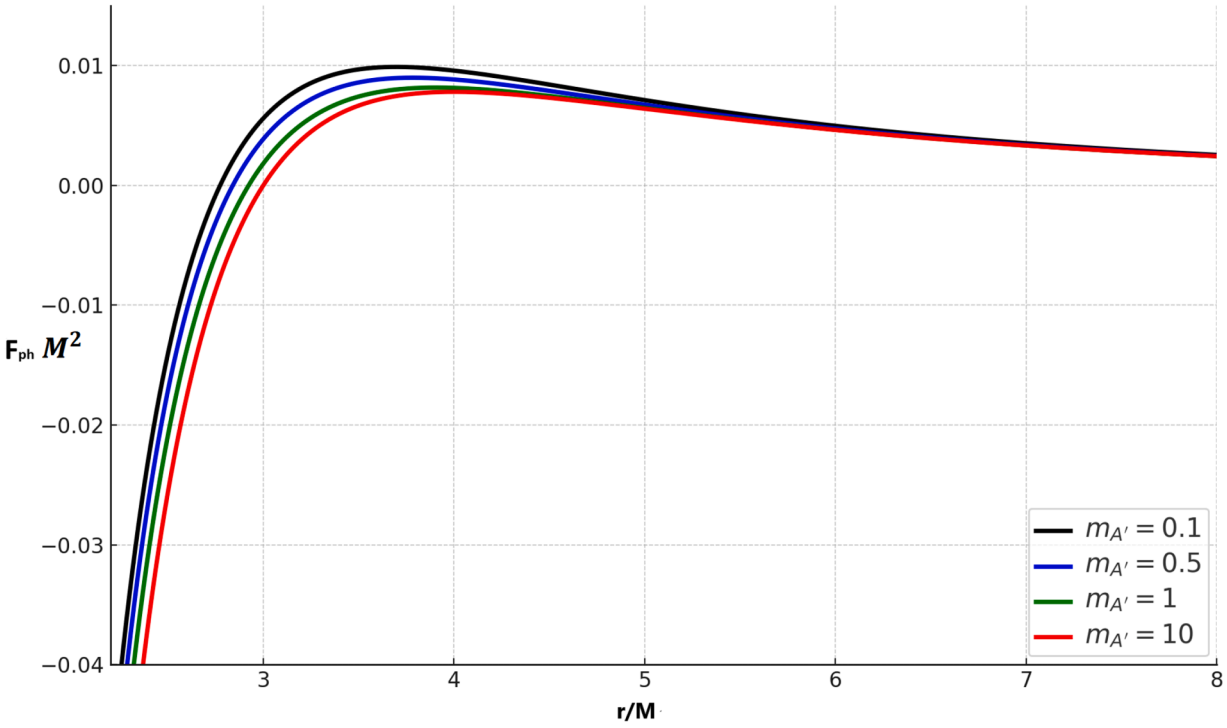

Fig. 5. The plot of force $F_{\rm ph}M^2$ on photon particle as a function of radial coordinate r/M for BH solutions in DPM for different values of $m_{A'}M$ for fixed $M = g_D = 0.5$, $\mu_f = S_{12} = 1$ and $\Lambda = 1.7$.

Next, we analyze the force exerted on a photon, focusing on the roles of the dark gauge coupling g_D and the dark photon mass $m_{A'}$. This force is represented in terms of the effective potential as

$$F_{\rm ph} = -\frac{1}{2}V'_{\rm eff}(r). \tag{27}$$

Using the expression for $V_{\rm eff}(r)$ from Eq. (23), we find the force to be

$$F_{\rm ph} = \frac{L^2}{r^3}\Big(2f(r) - rf'(r)\Big), \tag{28}$$

$$F_{\rm ph} = \frac{L^2}{r^3}\Bigg\{2 - \frac{4M}{r} + \frac{g_D^2}{\pi r}e^{-m_{A'}r}(m_{A'}r+1) - \frac{\mu_f^2 S_{12} m_{A'} e^{-m_{A'}r}}{\pi\Lambda^2 r^2} - \Bigg[\frac{2M}{r} + \frac{g_D^2}{2\pi}e^{-m_{A'}r}\Big(-\frac{1}{r}(m_{A'}r+1) - m_{A'}^2 r\Big) + \frac{\mu_f^2 S_{12} m_{A'} e^{-m_{A'}r}}{2\pi\Lambda^2}\Big(\frac{2}{r^2} + \frac{m_{A'}}{r}\Big)\Bigg]\Bigg\}. \tag{29}$$

This full expression relies on the derivatives of $f(r)$, with contributions from g_D and $m_{A'}$. Such corrections substantially influence whether the photon force behaves attractively or repulsively close to the BH. Eq. (29) describes the force acting on a photon in the gravitational field by the BH. This expression clearly shows that the force experienced by the massless photon is affected by various parameters, including the dark gauge coupling g_D and dark photon mass $m_{A'}$. Together, these parameters modify the effective potential, thereby altering the gravitational interaction that influences photon trajectories near the BH.

Figs. 5 to 7 illustrate the variation of the photon force $F_{\rm ph}$ as a function of radial distance r for BH solutions in DPM, with a particular focus on the effects of the dark photon mass $m_{A'}$ and the dark gauge coupling g_D. In Fig. 5, different values of $m_{A'}$ are analyzed while keeping g_D fixed. It is observed that as $m_{A'}$ increases, the magnitude of $F_{\rm ph}$ decreases and the peak of the repulsive force shifts slightly towards larger values of r, indicating that heavier dark photons suppress the strength of the effective force acting on photon trajectories. Fig. 6 examines the impact of varying g_D, where a higher coupling leads to an enhanced and more extended photon force profile. This suggests that the dark gauge interaction amplifies the gravitational influence of the BH, effectively increasing the deviation of null geodesics. Fig. 7 combines the effects of both $m_{A'}$ and g_D, revealing their nonlinear interplay: while g_D dominates the strength of the force, $m_{A'}$ controls its spatial attenuation via exponential decay. The mathematical modeling underlying these plots arises from the derivative of the effective potential $V_{\rm eff}(r)$, where both Yukawa-type and dipole contributions enter through $f(r)$ and its derivatives. Physically, these changes in $F_{\rm ph}$ demonstrate how dark photon fields reshape the near-horizon spacetime geometry, altering the behavior of photon orbits and the structure of the photon sphere. Fig. 8 provides a comparative illustration of the photon

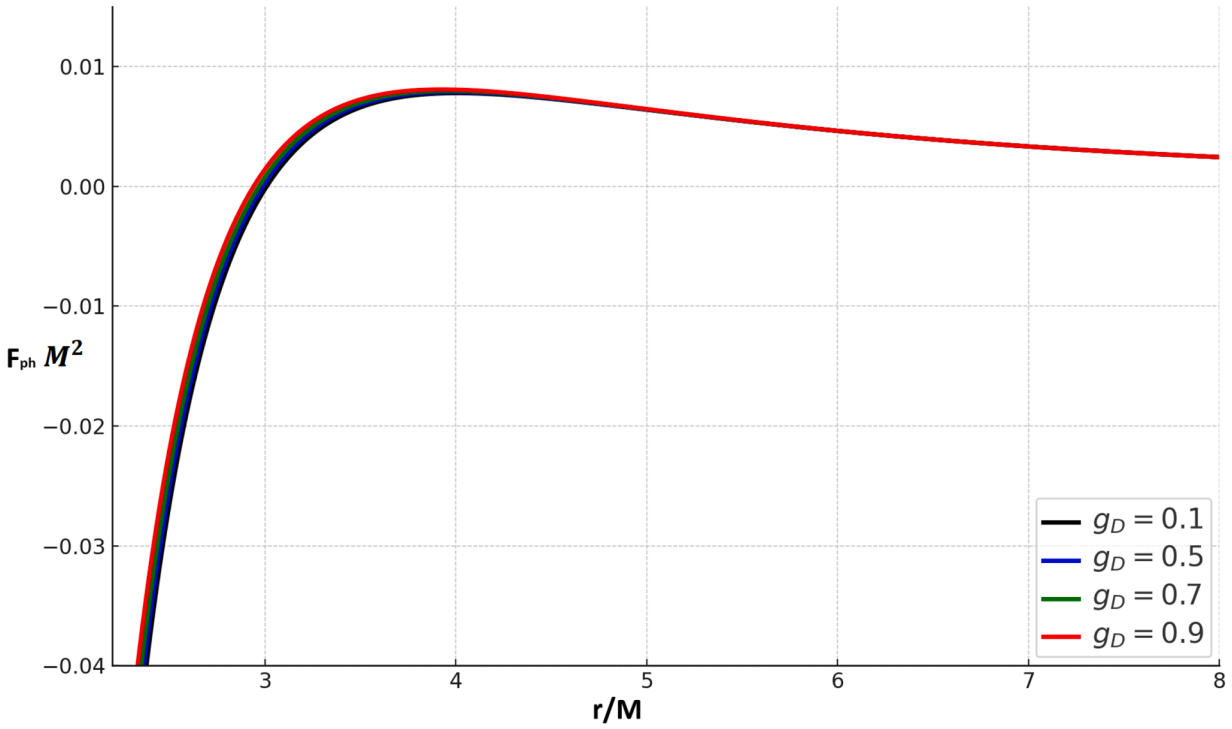

Fig. 6. The plot of force $F_{\text{ph}}M^2$ on photon particle as a function of radial coordinate r/M for BH solutions in DPM for different values of g_D for fixed $M = m_{A'}M = 0.5$, $\mu_f = S_{12} = 1$ and $\Lambda = 1.7$.

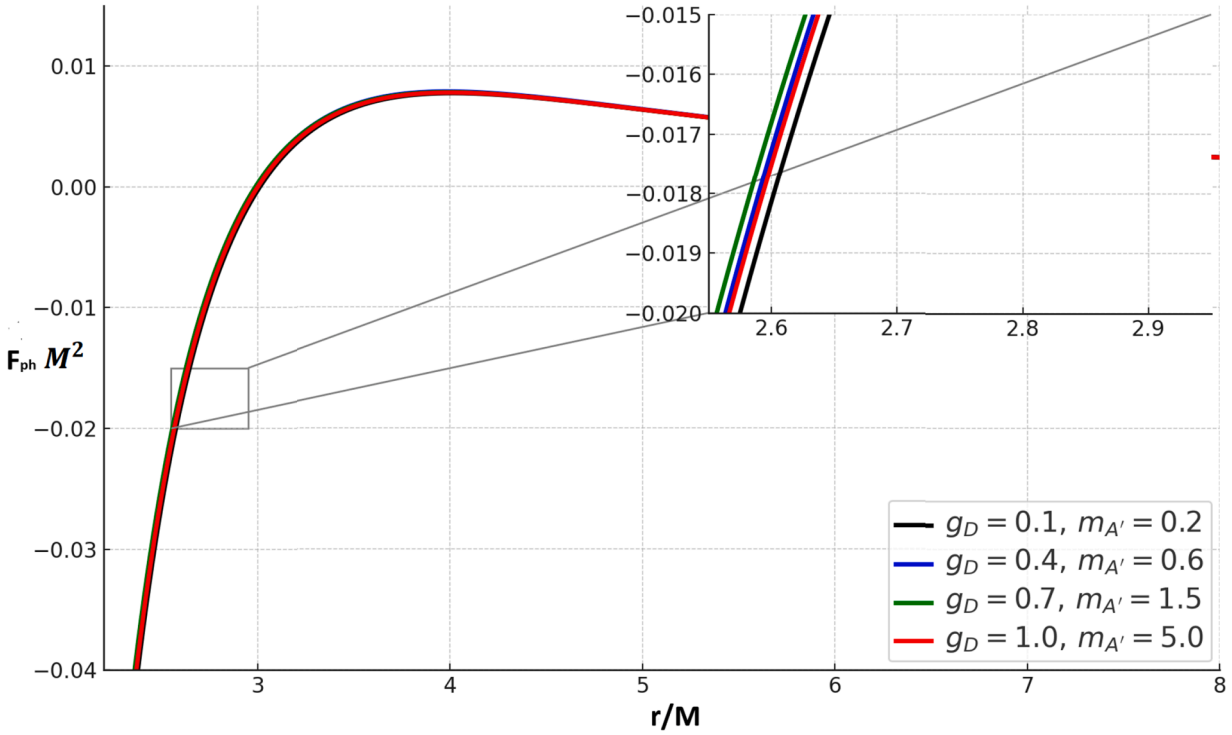

Fig. 7. The plot of force $F_{\text{ph}}M^2$ on photon particle as a function of radial coordinate r/M for BH solutions in DPM for different values of $m_{A'}M$ and g_D for fixed, $M = 0.5$, $\mu_f = S_{12} = 1$ and $\Lambda = 1.7$.

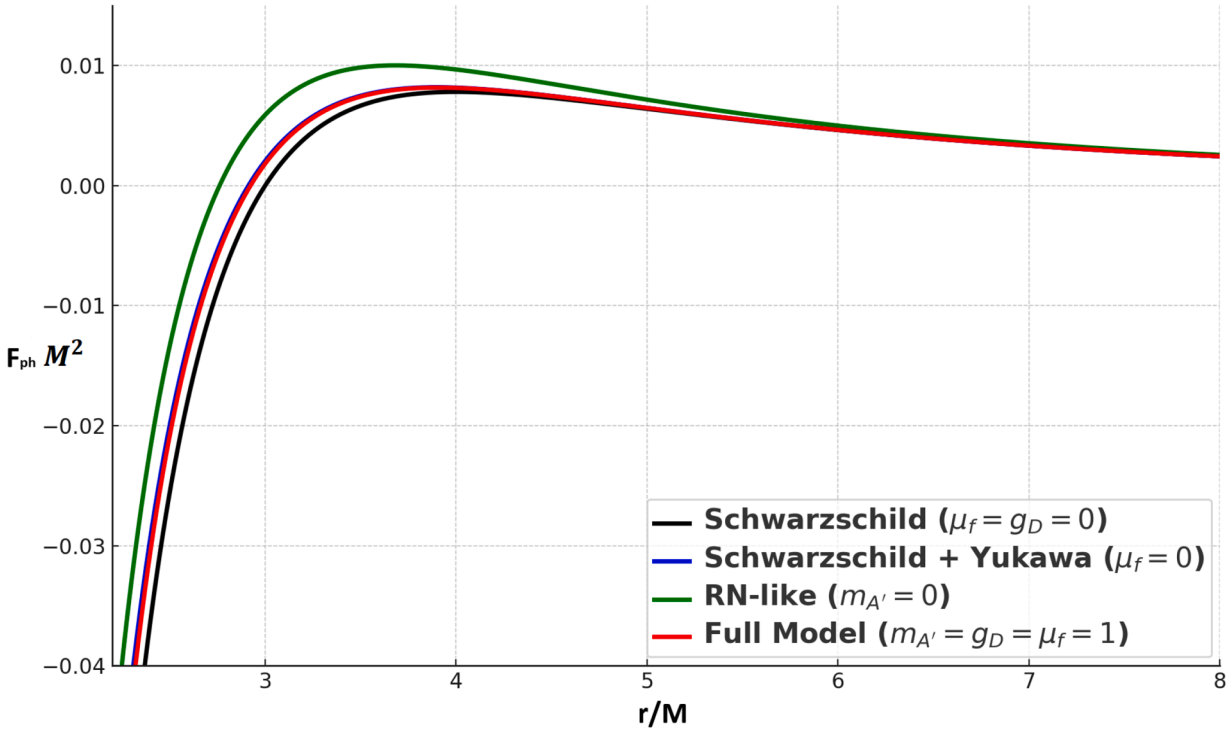

Fig. 8. The plot of force $F_{\rm ph}M^2$ on photon particle as a function of radial coordinate r/M for BH solutions in DPM, Schwarzschlid and RN-like BHs.

force $F_{\rm ph}$ as a function of radial coordinate r for solutions in DPMs alongside the classical Schwarzschild and RN-like BHs. The plot reveals that the inclusion of dark photon corrections introduces a significant deviation from the standard profiles of $F_{\rm ph}$ found in Schwarzschild and RN-like geometries. Specifically, the DPM exhibits a broader and more pronounced peak in the force curve, which indicates a stronger repulsive gravitational effect near the photon sphere. This enhancement is attributed to the exponential Yukawa-type and magnetic dipole corrections embedded in the metric function $f(r)$, which contribute additional terms to the gradient of the effective potential $V_{\rm eff}(r)$. Unlike the RN-like case, where the electromagnetic charge modifies the spacetime linearly, the dark photon corrections depend nonlinearly on the parameters g_D and $m_{A'}$, leading to richer and more tunable force profiles. The mathematical modeling shows that these corrections alter both the magnitude and spatial extent of the force acting on null particles, which in turn influences the curvature of light rays and the stability of photon orbits. Physically, this results in substantial changes in the BH's optical properties particularly its lensing behavior and shadow images.

We now calculate the period of circular orbits, defined as the time a particle takes to complete one full revolution along a circular timelike path. The expressions for the period in proper time (T_τ) and coordinate time (T_t) are derived in Ref. [23]. Using a similar method in our analysis, we find that the proper time period is

$$T_\tau = \frac{2\pi r_c^2}{L}. \tag{30}$$

In this expression r_c stands for the radius of the circular orbit, while L refers to the particle conserved angular momentum. The coordinate time period T_t, which corresponds to the time for a full orbit as seen by a distant observer is expressed as

$$T_t = 2\pi|\beta_c| = \sqrt{\frac{2\pi r_c}{f(r_c)}} = \sqrt{\frac{2\pi r_c}{1 - \frac{2M}{r_c} + \frac{g_D^2}{2\pi}\frac{e^{-m_{A'}r_c}(m_{A'}r_c+1)}{r_c} - \frac{\mu_f^2 S_{12} m_{A'} e^{-m_{A'}r_c}}{2\pi\Lambda^2 {r_c}^2}}}, \tag{31}$$

here r_c is the radius of the circular orbit, obtained by solving Eq. (26). Next, we turn our attention to the Lyapunov exponent which is a key physical quantity that indicates the stability of a circular orbit and it is defined as [22]

$$\lambda_L^{\rm null} = \sqrt{-\frac{V''_{\rm eff}}{2\dot{t}^2}}. \tag{32}$$

Using Eq. (19), the null geodesics effective potential (23), and the condition for photon spheres (26), we obtain a clear formula for the Lyapunov exponent

$$\lambda_L^{\text{null}} = \sqrt{f(r_c)\left(\frac{f(r_c)}{r_c^2} - \frac{f''(r_c)}{2}\right)}. \tag{33}$$

Finally, substituting the metric function $f(r)$ from Eq. (14), we obtain

$$\begin{aligned}\lambda_L^{\text{null}} =& \frac{1}{4\pi^{3/2}}\Bigg(-\frac{1}{\Lambda^6 r^{10}}\left(e^{-3m_{A'}r}\left(\Lambda^2 r(g_D^2 + 2\pi e^{m_{A'}r}(r-2M)) + m_{A'}(g_D^2\Lambda^2 r^2 - S_{12}u^2)\right)^2 (m_{A'}{}^3(r^2 S_{12}\mu_f^2 \right.\\ & \left. - g_D^2\Lambda^2 r^4) + m_{A'}{}^2(4rS_{12}\mu_f^2 - g_D^2\Lambda^2 r^3) - 2\Lambda^2 r(g_D^2 - 4\pi M e^{m_{A'}r}) + m_{A'}(6S_{12}\mu_f^2 - 2g_D^2\Lambda^2 r^2))\right)\Bigg)^{\frac{1}{2}}.\end{aligned} \tag{34}$$

Eq. (34) clearly shows that various parameters such as the dark gauge coupling g_D and the dark photon mass $m_{A'}$ have a significant impact on the Lyapunov exponent, and thus on the stability of circular photon orbits. A higher Lyapunov exponent corresponds to greater instability under radial perturbations.

3.2. Timelike geodesics and ISCO analysis

In this section, we analyze the motion of massive test particles and investigate the effects of the dark gauge coupling g_D on their timelike trajectories. For timelike geodesics, we set $\kappa = -1$, reducing the effective potential in Eq. (22) to

$$V_{\text{eff}}(r) = \left(1 + \frac{L^2}{r^2}\right)\left[1 - \frac{2M}{r} + \frac{g_D^2}{2\pi r}e^{-m_{A'}r}(m_{A'}r + 1) - \frac{\mu_f^2 S_{12} m_{A'} e^{-m_{A'}r}}{2\pi\Lambda^2 r^2}\right]. \tag{35}$$

Circular orbits occur when a test particle remains at a constant radial distance r from the . Whether these orbits are stable or unstable is determined by the behavior of the effective potential $V_{\text{eff}}(r)$. The essential requirement for circular orbits is that both the radial velocity and radial acceleration are zero, meaning $\dot{r} = \ddot{r} = 0$, or equivalently $u^r = \dot{u}^r = 0$. Therefore, the following two conditions need to be met for circular orbits

$$E^2 = V_{\text{eff}}(r), \qquad \frac{dV_{\text{eff}}}{dr} = 0. \tag{36}$$

By solving these conditions simultaneously and applying the metric equation, the total energy E, the total angular momentum L, and the angular velocity $\Omega \equiv \frac{d\phi}{dt} = \frac{u^\phi}{u^t}$ of the test particle in the background of a loop quantum are expressed as

$$E^2 = \frac{2f^2(r)}{2f(r) - rf'(r)}, \tag{37}$$

Figs. 9 to 12 depict the behavior of the effective potential $V_{\text{eff}}(r)$ for time-like geodesics in spacetimes influenced by DPM, highlighting the effects of varying dark photon mass $m_{A'}$ and dark gauge coupling g_D. Fig. 9 demonstrates that an increase in $m_{A'}$ results in a decrease in the height of the effective potential and a slight outward shift in the location of its minimum. This indicates that heavier dark photons weaken the attractive gravitational pull experienced by massive particles and increase the orbital radius of stable circular motion. Conversely, Fig. 10 shows that increasing g_D significantly raises the potential's height and shifts the minimum to smaller radial distances, implying stronger gravitational attraction and more tightly bound orbits. Fig. 11 provides a combined view of the impact of both $m_{A'}$ and g_D, confirming that their interplay govern the depth and position of the potential well, which is crucial for determining orbital stability and energetics of test particles. Fig. 12 offers a comparative analysis between dark photon BHs and classical Schwarzschild and RN-like solutions, revealing that the DPM yields a deeper and narrower potential well, suggesting more compact and energetically stable orbits. These variations in $V_{\text{eff}}(r)$ stem from modifications to the lapse function $f(r)$ due to Yukawa and dipole terms, which introduce novel curvature effects into the spacetime geometry. Physically, these findings indicate that dark photon fields significantly alter the orbital structure around BHs, affecting key astrophysical processes such as accretion dynamics, energy emission rates, and ISCO behavior. The altered geodesic profiles also influence the gravitational redshift and potential observational signals from orbiting matter, offering a pathway to constrain dark sector physics via precision observations.

$$\begin{aligned}E^2 =& \left[4\pi\Lambda^2 M r_c\, e^{m_{A'}r_c} - \Lambda^2 g_D^2 r_c(m_{A'}r_c + 1) - 2\pi\Lambda^2 r_c^2\, e^{m_{A'}r_c} + S_{12}m_{A'}\mu_f^2\right]^2 e^{-m_{A'}r_c}\left(\pi\Lambda^2 r_c^2\left[8\pi\Lambda^2 M r_c\, e^{m_{A'}r_c}\right.\right.\\ & - 2\Lambda^2 g_D^2 r_c(m_{A'}r_c + 1) - 4\pi\Lambda^2 r_c^2\, e^{m_{A'}r_c} + 2S_{12}m_{A'}\mu_f^2 + r_c^2\Big(4\pi\Lambda^2 M r_c\, e^{m_{A'}r_c} + \Lambda^2 g_D^2 r_c(m_{A'}^2 r_c^2 + m_{A'}r_c + 1)\\ & \left.\left. - S_{12}m_{A'}\mu_f^2(m_{A'}r_c + 2)\Big)\right]\right)^{-1}\end{aligned}$$

Figs. 13 to 16 illustrate the behavior of the energy of time-like particles in stable circular orbits around BHs in DPMs, as a function of the radial coordinate r, for various values of the dark photon mass $m_{A'}$ and the dark gauge coupling g_D. In Fig. 13, we observe that increasing $m_{A'}$ leads to a slight upward shift in the energy profile and a displacement of the energy minimum to larger radial

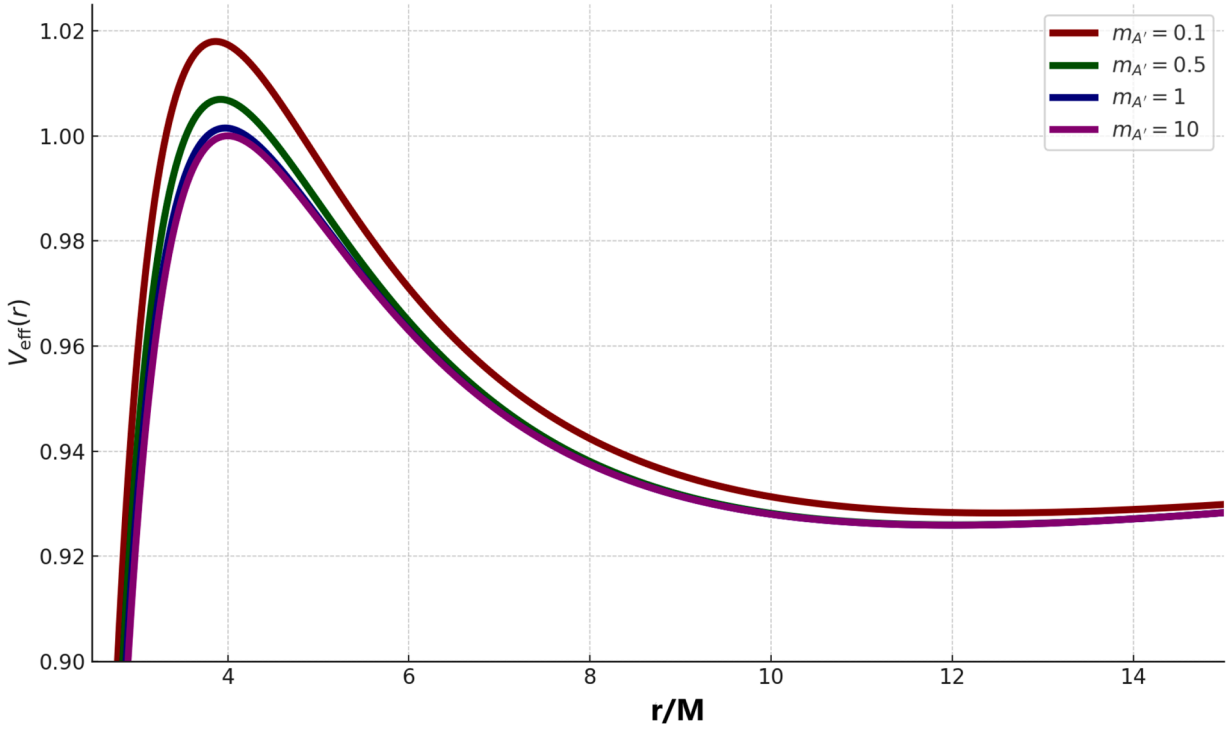

Fig. 9. The plot of effective potential $V_{\text{eff}}(r)$ for time-like geodesics as a function of radial coordinate r/M for BH solutions in DPM for different values of $m_{A'}M$ for fixed $M = g_D = 0.5$, $\mu_f = S_{12} = 1$ and $\Lambda = 1.7$.

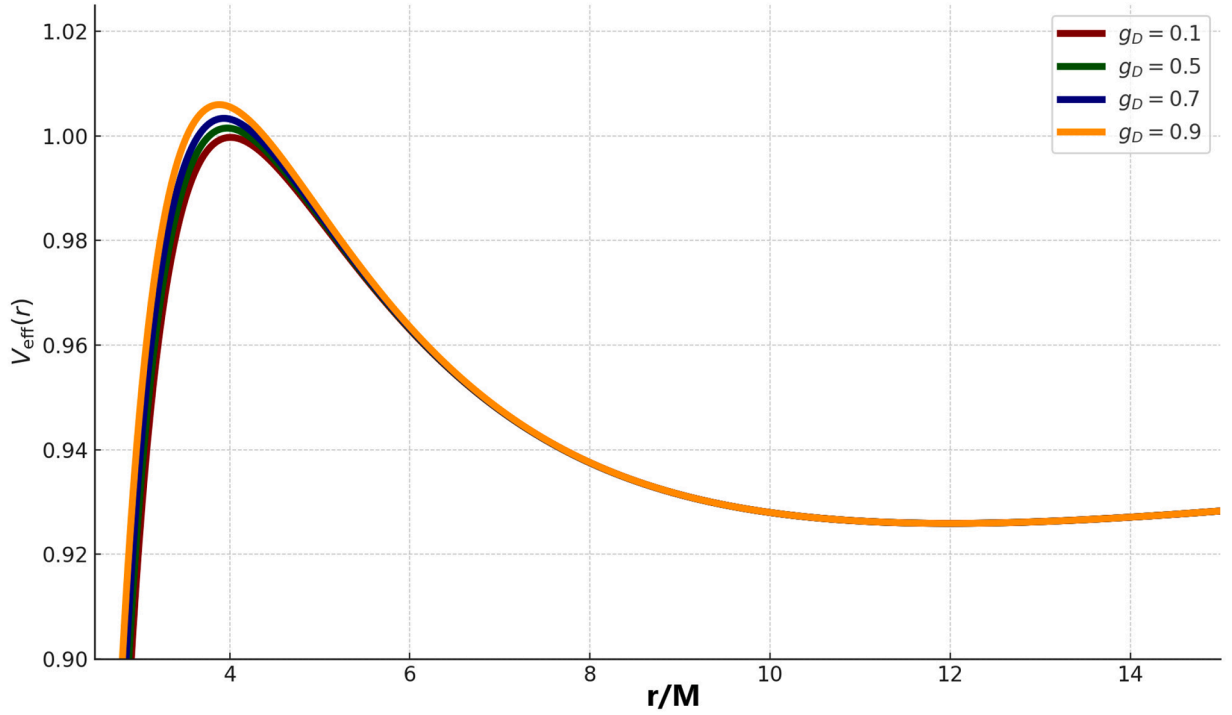

Fig. 10. The plot of effective potential $V_{\text{eff}}(r)$ for time-like geodesics as a function of radial coordinate r/M for BH solutions in DPM for different values of g_D for fixed $M = m_{A'}M = 0.5$, $\mu_f = S_{12} = 1$ and $\Lambda = 1.7$.

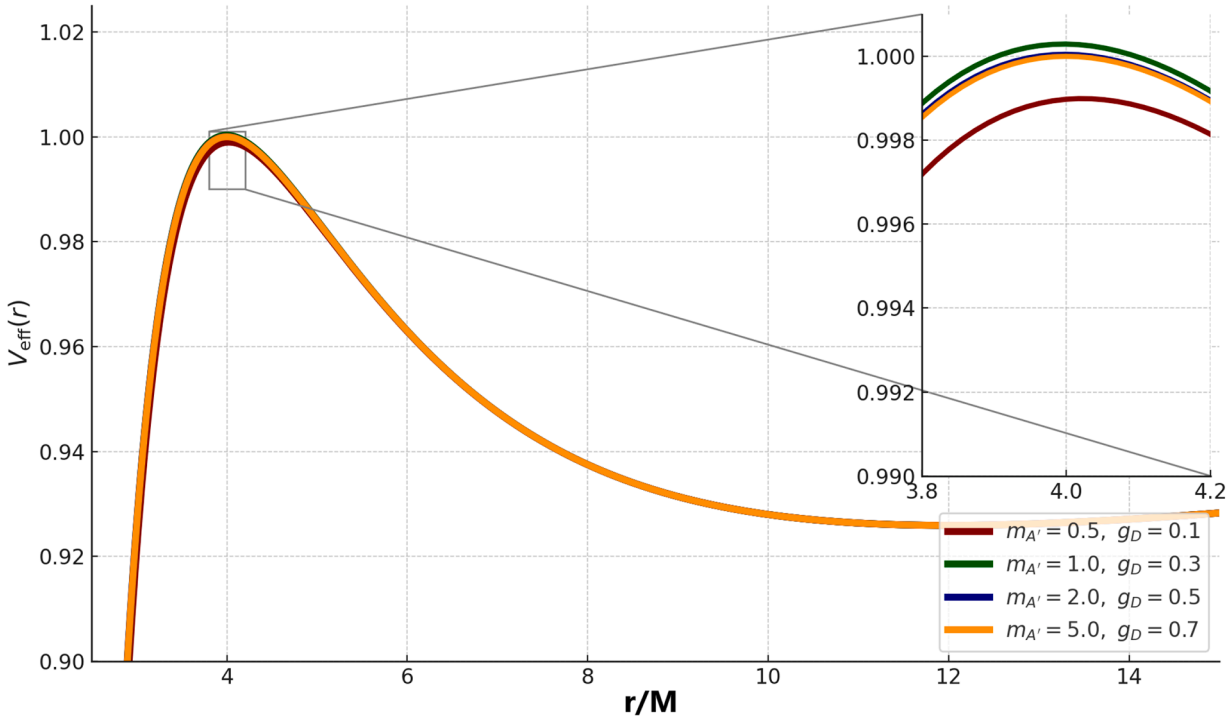

Fig. 11. The plot of effective potential $V_{\text{eff}}(r)$ for time-like geodesics as a function of radial coordinate r/M for BH solutions in DPM for different values of $m_{A'}M$ and g_D for fixed, $M = 0.5$, $\mu_f = S_{12} = 1$ and $\Lambda = 1.7$.

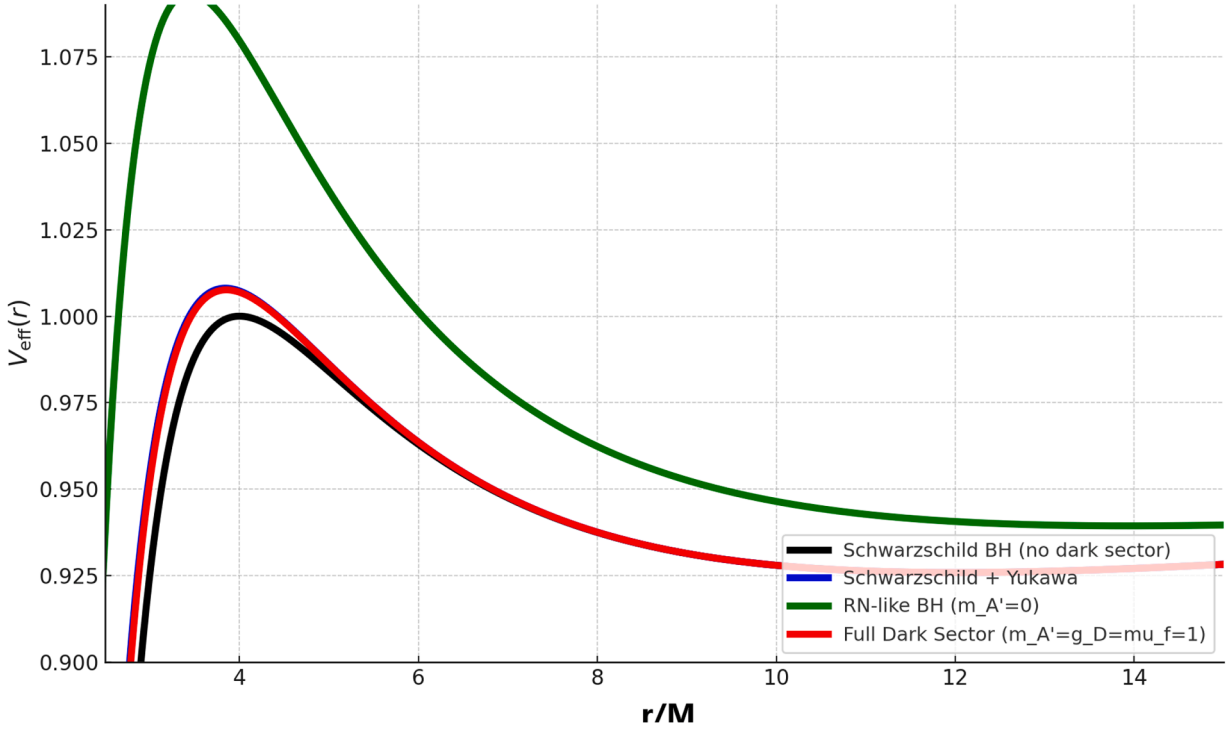

Fig. 12. The plot of effective potential $V_{\text{eff}}(r)$ for time-like geodesics as a function of radial coordinate r/M for BH solutions in DPM, Schwarzschlid and RN-LIKE BHs.

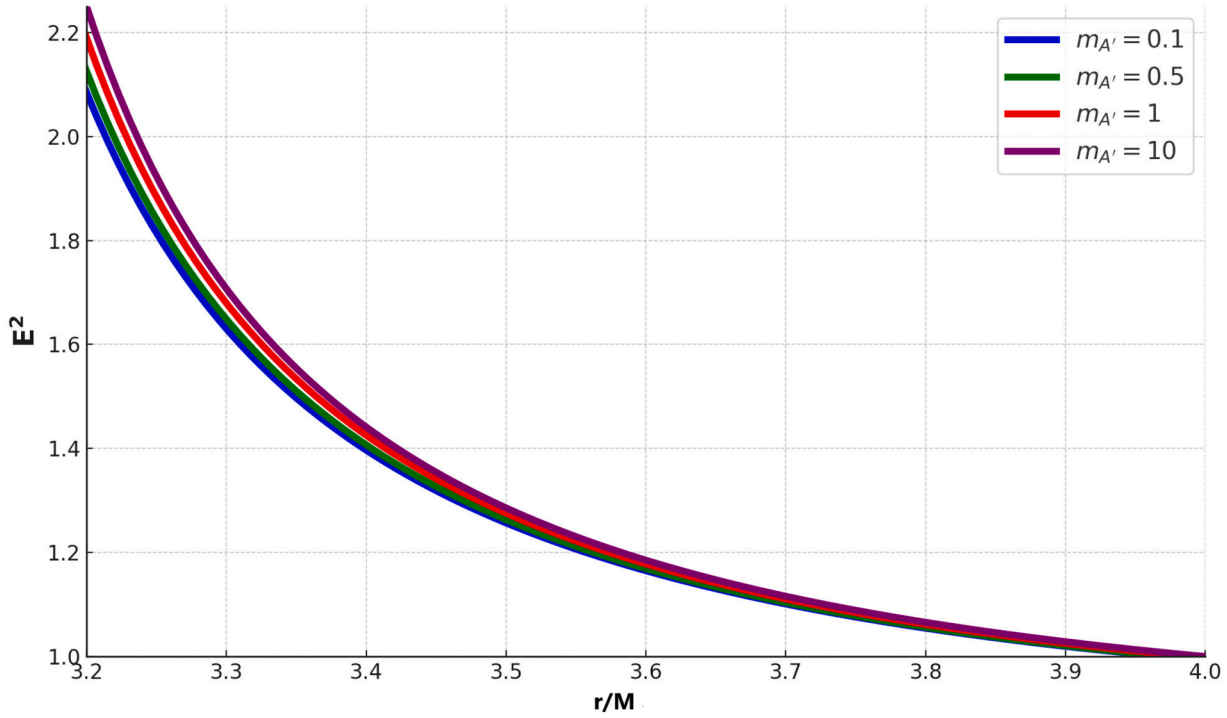

Fig. 13. The plot of energy E^2 as a function of radial coordinate r/M for BH solutions in DPM for different values of $m_{A'}M$ for fixed $M = g_D = 0.5$, $\mu_f = S_{12} = 1$ and $\Lambda = 1.7$.

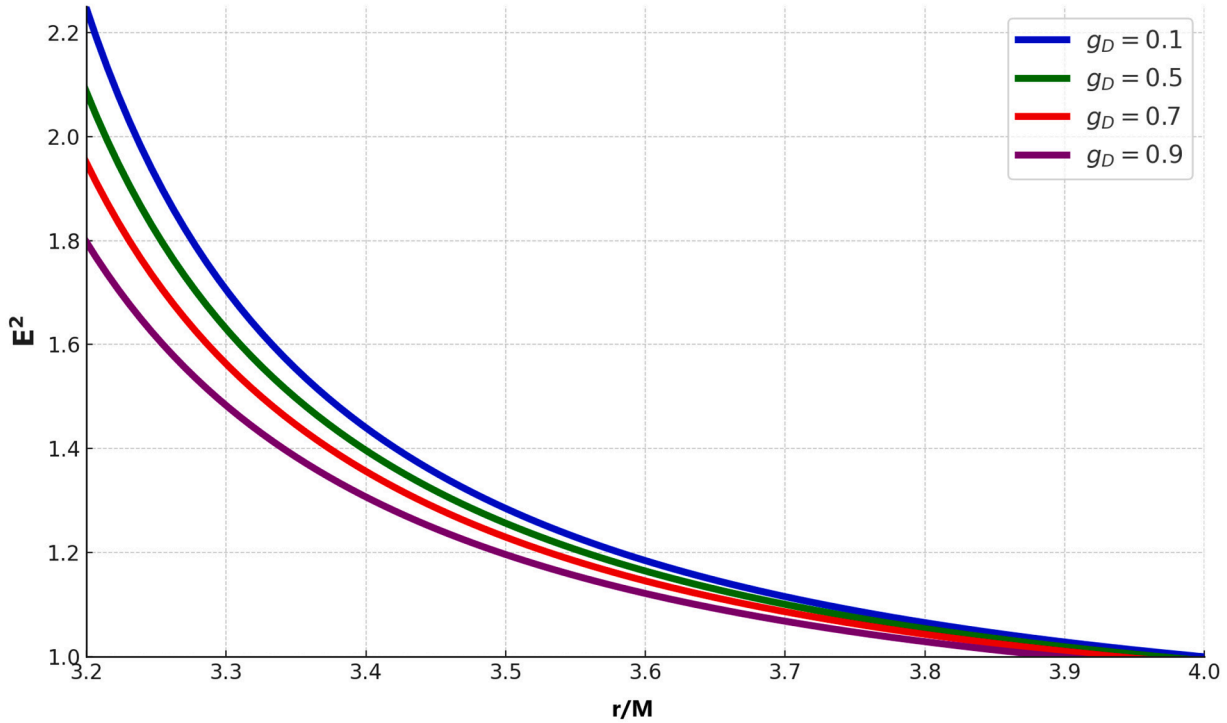

Fig. 14. The plot of energy E^2 as a function of radial coordinate r/M for BH solutions in DPM for different values of g_D for fixed $M = m_{A'}M = 0.5$, $\mu_f = S_{12} = 1$ and $\Lambda = 1.7$.

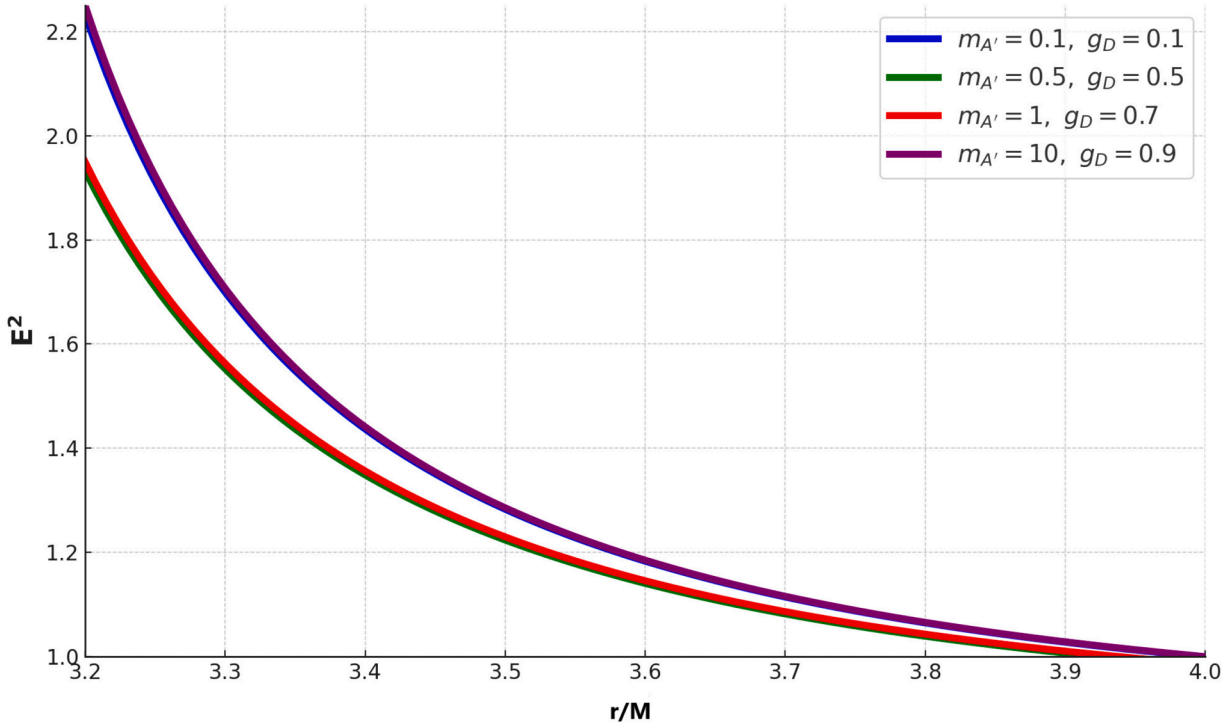

Fig. 15. The plot of energy E^2 as a function of radial coordinate r/M for BH solutions in DPM for different values of $m_{A'}M$ and g_D for fixed $M = 0.5$, $\mu_f = S_{12} = 1$ and $\Lambda = 1.7$.

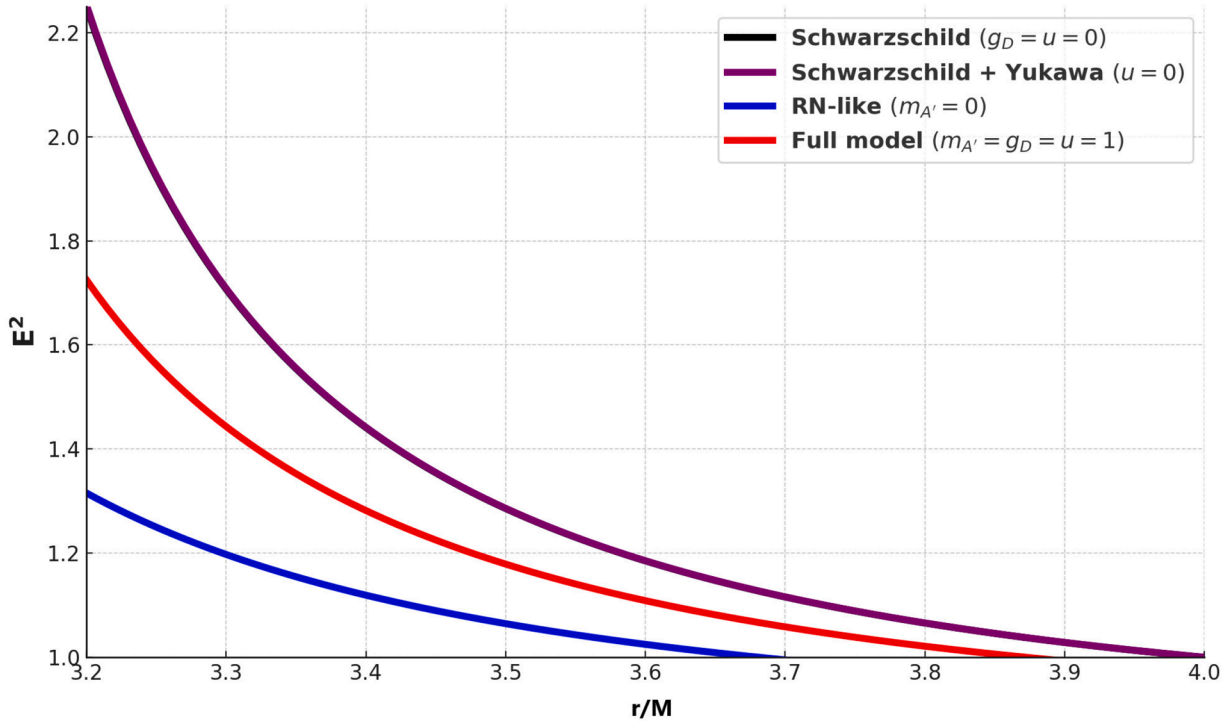

Fig. 16. The plot of energy E^2 as a function of radial coordinate r/M for BH solutions in DPM, Schwarzschlid and RN-like BHs.

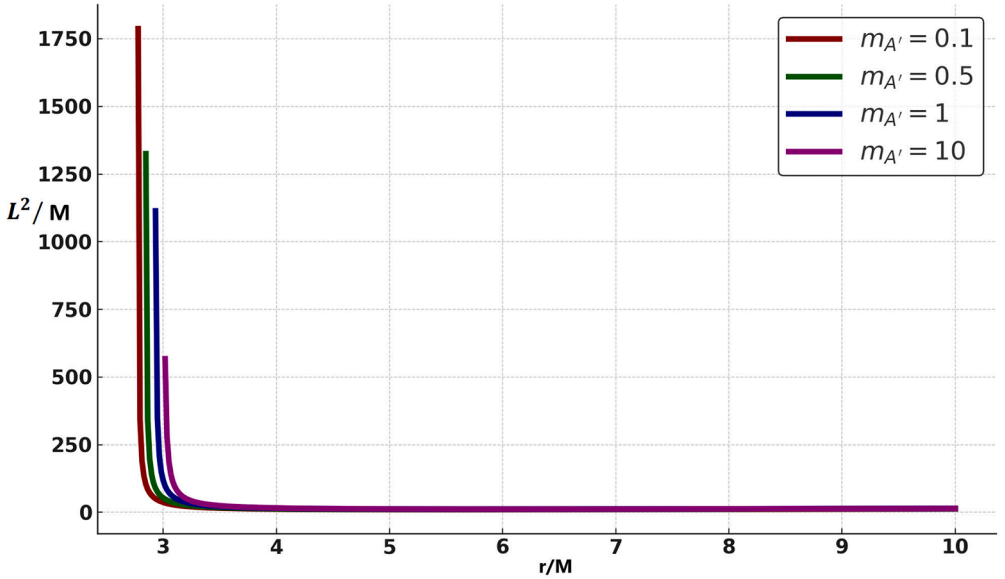

Fig. 17. The plot of angular momentum L^2/M as a function of radial coordinate r/M for BH solutions in DPM for different values of $m_{A'}M$ for fixed $M = g_D = 0.5$, $\mu_f = S_{12} = 1$ and $\Lambda = 1.7$.

distances, indicating that heavier dark photons weaken the gravitational binding of particles and push stable orbits outward. Fig. 14 shows the opposite trend with respect to g_D: as the coupling strength increases, E^2 decreases and the potential well deepens, which suggests more energetically favorable orbits and stronger gravitational attraction due to enhanced interaction with the dark photon field. Fig. 15 captures the combined influence of both $m_{A'}$ and g_D, revealing that while $m_{A'}$ tends to broaden and elevate the energy profile, g_D acts to deepen and localize it. Fig. 16 provides a comparative analysis with Schwarzschild and RN-like geometries, highlighting that the DPM predicts significantly different energy profiles typically deeper and occurring at smaller orbital radii due to the exponential corrections from Yukawa-type and magnetic dipole interactions in the metric function $f(r)$. These modifications in E^2 directly influence the energetics of matter orbiting the BH, affecting the ISCO location, energy release efficiency, and overall accretion dynamics. Consequently, the presence of dark photon interactions leads to measurable deviations in observable phenomena such as thermal spectra, quasiperiodic oscillations, and gravitational wave signatures.

$$L^2 = \frac{r^3 f'(r)}{2f(r) - rf'(r)}, \tag{38}$$

$$L^2 = \left(r_c^4\left[-4\pi\Lambda^2 M r_c e^{m_{A'}r_c} - \Lambda^2 g_D^2 r_c\left(m_{A'}^2 r_c^2 + m_{A'} r_c + 1\right) + S_{12} m_{A'} \mu_f^2 (m_{A'} r_c + 2)\right]\right)\left(8\pi\Lambda^2 M r_c e^{m_{A'}r_c} - 2\Lambda^2 \right.$$
$$\times g_D^2 r_c (m_{A'} r_c + 1) - 4\pi\Lambda^2 r_c^2 e^{m_{A'}r_c} + 2S_{12} m_{A'} \mu_f^2 + r_c^2\left[4\pi\Lambda^2 M r_c e^{m_{A'}r_c} + \Lambda^2 g_D^2 r_c (m_{A'}^2 r_c^2 + m_{A'} r_c + 1) - S_{12}\right.$$
$$\left.\left.\times m_{A'} \mu_f^2 (m_{A'} r_c + 2)\right]\right)^{-1}.$$

Figs. 17 to 20 display the angular momentum as a function of radial coordinate r for time-like particles in circular orbits around BH influenced by dark photon fields. Fig. 17 shows that increasing the dark photon mass $m_{A'}$ leads to a rise in the peak of the L^2 curve and a corresponding outward shift in the orbital radius, indicating that heavier dark photons reduce the gravitational binding and require more angular momentum to sustain circular orbits at larger radii. In contrast, Fig. 18 highlights that an increase in the dark gauge coupling g_D causes a noticeable decrease in the required angular momentum and contracts the radius of stable orbits, signifying enhanced gravitational strength due to stronger interaction with the dark photon field. Fig. 19 examines the combined effects of both $m_{A'}$ and g_D, confirming that their interplay nonlinearly controls the angular momentum distribution where g_D dominates the compactness and $m_{A'}$ modulates the spatial extension. Fig. 20 compares the dark photon solutions with classical Schwarzschild and RN-like BH, demonstrating that the DPM results in significantly lower angular momentum thresholds for stable orbits, owing to the inclusion of exponential Yukawa and spin-spin dipole corrections in the metric function $f(r)$. These theoretical insights derived from the geodesic equations reflect profound changes in the orbital mechanics around the BH. Physically, the variations in L^2 affect the structure of accretion disks, the frequency of emitted radiation, and the dynamics of infalling matter.

$$\Omega_\phi{}^2 = \frac{1}{2r} f'(r). \tag{39}$$

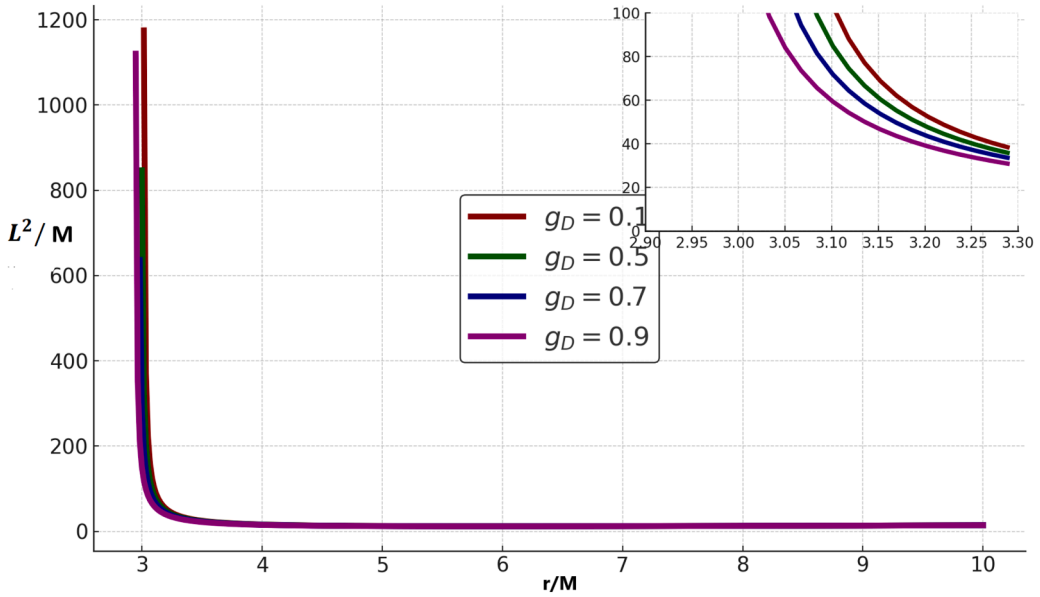

Fig. 18. The plot of angular momentum L^2/M as a function of radial coordinate r/M for BH solutions in DPM for different values of g_D for fixed $M = m_{A'}M = 0.5$, $\mu_f = S_{12} = 1$ and $\Lambda = 1.7$.

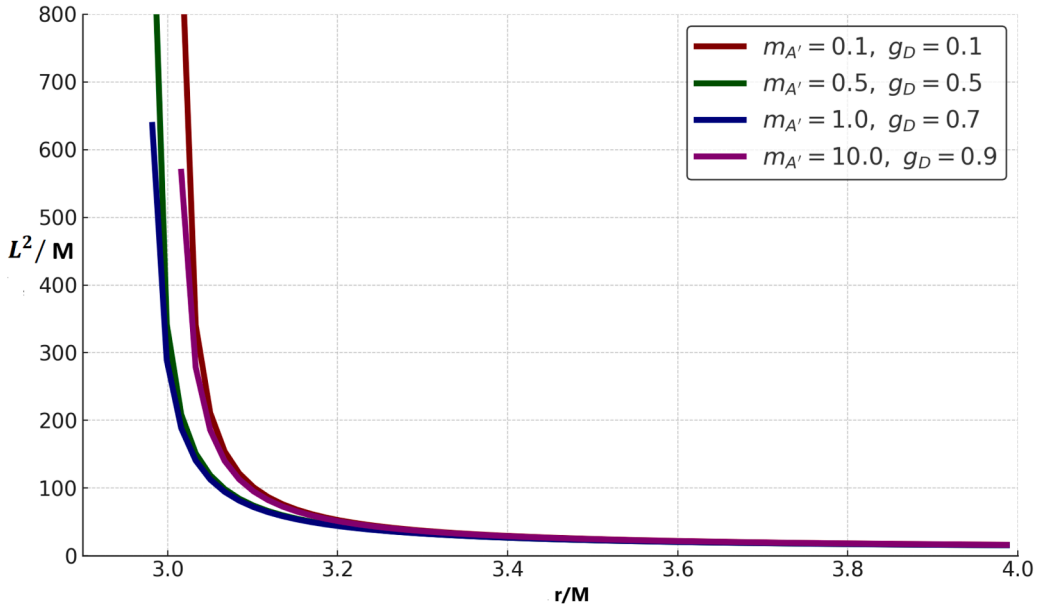

Fig. 19. The plot of angular momentum L^2/M as a function of radial coordinate r/M for BH solutions in DPM for different values of $m_{A'}M$ and g_D for fixed $M = 0.5$, $\mu_f = S_{12} = 1$ and $\Lambda = 1.7$.

Putting all the value in Eq. (39)

$$\Omega_\phi{}^2 = (e^{-m_{A'}r}\left(m_{A'}{}^2\left(rS_{12}\mu_f^2 - g_D{}^2\Lambda^2r^3\right) - \Lambda^2r\left(g^2 - 4\pi M e^{m_{A'}r}\right) + m_{A'}\left(2S_{12}\mu_f^2 - g_D{}^2\Lambda^2r^2\right)\right))(4\pi\Lambda^2r^4)^{-1}$$

To ensure orbital stability, the effective potential $V_{\text{eff}}(r)$ must not only satisfy the conditions for circular orbits but also exhibit a local minimum. This leads to the condition [24]

$$\frac{d^2V_{\text{eff}}}{dr^2} > 0, \tag{40}$$

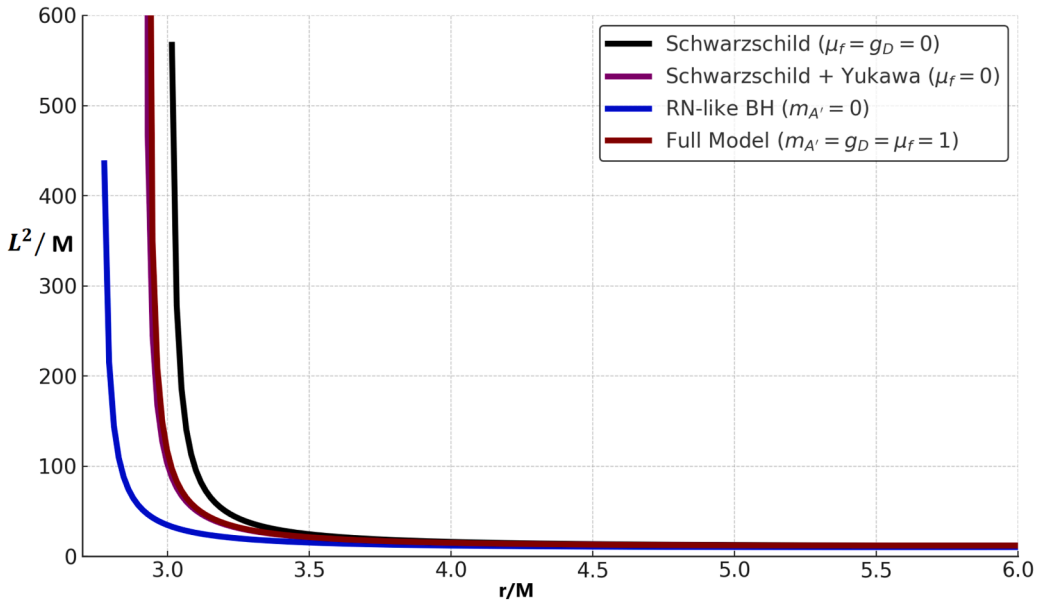

Fig. 20. The plot of angular momentum L^2/M as a function of radial coordinate r/M for BH solutions in DPM, Schwarzschlid and RN-like BHs.

this ensures that small radial disturbances cause oscillations that remain confined around the circular orbit. In contrast, if the circular orbit corresponds to a local maximum of the effective potential, it is unstable to radial perturbations. This is expressed by the condition

$$\frac{d^2V_{\text{eff}}}{dr^2} < 0. \tag{41}$$

The transition between stable and unstable circular orbits is indicated by the point where the second derivative equals zero

$$\frac{d^2V_{\text{eff}}}{dr^2} = 0, \tag{42}$$

which defines the ISCO. The ISCO is crucial in astrophysical processes, especially in the dynamics of accretion disks, as it represents the smallest radius at which a massive test particle can maintain stable circular motion. At this orbit, the effective potential simultaneously satisfies the following critical conditions [24]

$$\frac{dV_{\text{eff}}}{dr} = 0, \qquad \frac{d^2V_{\text{eff}}}{dr^2} = 0. \tag{43}$$

The presence of the ISCO radius r_{ISCO} arises purely from relativistic effects. In contrast to classical mechanics where the effective potential generally features a single global minimum general relativity allows for more complex behavior, including the existence of both a local maximum and a local minimum, or in some cases, the absence of any extrema altogether, depending on the angular momentum L. The relativistic form of the effective potential enables both an unstable inner circular orbit and a stable outer circular orbit to exist simultaneously. The ISCO represents the radius at which these two orbits coincide. In other words, for a given angular momentum L, the ISCO marks the critical boundary beyond which stable circular orbits are no longer possible. For the considered model, the intricate form of the metric function prevents the derivation of an explicit analytical expression for the ISCO. Consequently, the equation set (43) must be solved numerically to determine the ISCO radius r_{ISCO}, as well as the corresponding angular momentum L_{ISCO} and energy E_{ISCO} for a test particle in such a geometry. The smaller ISCO radius generally allows the inner edge of the disk to extend deeper into the gravitational potential well of the BH, thereby increasing the efficiency of energy extraction. This manifests observationally as a harder and more luminous spectrum, with shifts in the high-energy tail of the thermal component. Conversely, an outward shift of the ISCO radius reduces the efficiency of accretion, leading to comparatively softer spectra with diminished X-ray flux. Since the ISCO position and binding energy are directly altered by the dark photon parameters $m_{A'}$ and g_D, these modifications can, in principle, be probed through precision modeling of accretion disk spectra around astrophysical BHs. Tables 1–3 lists the numerically obtained values of r_{ISCO}, L_{ISCO}, and E_{ISCO} for dark gauge coupling g_D and dark photon mass $m_{A'}$

The motion of a test particle around can be described by the relationship between the radial coordinate r and the azimuthal angle ϕ. This relation can be obtained from the geodesic equation which is expressed as

$$\left(\frac{dr}{d\phi}\right)^2 = \frac{r^4}{L^2}\left[E^2 - f(r)\left(1 + \frac{L^2}{r^2}\right)\right], \tag{44}$$

Table 1
Numerical values of $r_{\rm ISCO}/M$, $E_{\rm ISCO}$, and $L_{\rm ISCO}/M$ for a test particle in the spacetime of a Dark Photon with higher-order corrections, for different values of $m_{A'}M$. (We set $M = 1$).

$m_{A'}M$	$r_{\rm ISCO}/M$	$E_{\rm ISCO}$	$L_{\rm ISCO}/M$
0.1	5.7920	0.941060	3.381132
0.5	5.9455	0.942543	3.447410
1.0	5.9914	0.942775	3.462516
10.0	6.0000	0.942809	3.464102

Table 2
Numerical values of $r_{\rm ISCO}/M$, $E_{\rm ISCO}$, and $L_{\rm ISCO}/M$ for a test particle in the spacetime of a Dark Photon with higher-order corrections, for different values of g_D. Fixed parameters are $m_{A'}M = 1.0$, $\mu_f = 5.0$, $S_{12} = 2.0$, and $\Lambda = 0.5$ (with $M = 1$).

g_D	$r_{\rm ISCO}/M$	$E_{\rm ISCO}$	$L_{\rm ISCO}/M$
0.1	4.2462	0.924890	3.547918
0.5	4.2229	0.924439	3.548076
0.7	4.1993	0.923967	3.548252
0.9	4.1677	0.923300	3.548506

Table 3
Numerical values of $r_{\rm ISCO}/M$, $E_{\rm ISCO}$, and $L_{\rm ISCO}/M$ for a test particle in the spacetime of a Dark Photon with higher-order corrections, for different combinations of $m_{A'}M$ and g_D. Fixed parameters are $\mu_f = 5.0$, $S_{12} = 2.0$, $\Lambda = 0.5$, and $M = 1$.

$m_{A'}M$	g_D	$r_{\rm ISCO}/M$	$E_{\rm ISCO}$	$L_{\rm ISCO}/M$
0.1	0.1	7.3362	0.947053	3.901575
0.5	0.5	4.9875	0.910956	3.572478
1.0	0.7	4.1993	0.923967	3.548252
10.0	0.9	6.0000	0.942809	3.464102

where $f(r)$ denotes the lapse function, E and L represent the particles specific energy and specific angular momentum, respectively. By numerically solving Eq. (44), the resulting trajectories can be visualized in Cartesian coordinates using the following transformations

$$x = r\cos\phi, \quad y = r\sin\phi.$$

Figs. 21 and 22 depict the trajectories of test particles in the equatorial plane around BHs influenced by dark photon fields, emphasizing the effects of varying dark photon mass $m_{A'}$ and dark gauge coupling g_D, respectively. In Fig. 21, the trajectories corresponding to different values of $m_{A'}$ reveal that as the mass of the dark photon increases, the particle orbits have no significant effects. In contrast, Fig. 22 illustrates that increasing g_D enhances the gravitational interaction, leading to more compact and tightly wound trajectories, with particles exhibiting greater angular rotation and reduced radial displacement. These pattern are direct consequences of the corrections embedded in the metric function $f(r)$, where Yukawa-type and magnetic dipole terms significantly alter the geodesic structure. Physically, these trajectory modifications imply that the presence of dark photon interactions reshapes the spacetime curvature near the BH, influencing how particles move in its vicinity. We now define the orbital velocity $\Omega(r)$ for test particles moving in circular orbits as

$$\Omega(r) \equiv \frac{\dot{\phi}}{\dot{t}}, \tag{45}$$

$$\Omega(r) \equiv \sqrt{\frac{e^{-m_{A'}r}\left(m_{A'}{}^2\left(rS_{12}\mu_f^2 - g_D{}^2\Lambda^2r^3\right) - \Lambda^2 r\left(g_D{}^2 - 4\pi M e^{m_{A'}r}\right) + m_{A'}\left(2S_{12}\mu_f^2 - g_D{}^2\Lambda^2r^2\right)\right)}{4\pi\Lambda^2r^3}}.$$

Figs. 23 to 26 illustrate the variation of orbital velocity $\Omega(r)$ of test particles in circular motion around BH under the influence of dark photon fields, with emphasis on the role of the dark photon mass $m_{A'}$ and dark gauge coupling g_D. In Fig. 23, increasing values of $m_{A'}$ are shown to cause a monotonic increase in $\Omega(r)$, particularly in the near-horizon region, signifying a strong gravitational pull due to stronger exponential effects in the Yukawa-type interaction. This reflects the increased curvature and delayed orbital acceleration in spacetimes dominated by heavier dark photons. Conversely, Fig. 24 demonstrates that an increase in g_D results in lower orbital velocities at all radii, implying an enhancement of the effective gravitational field strength due to the dark gauge

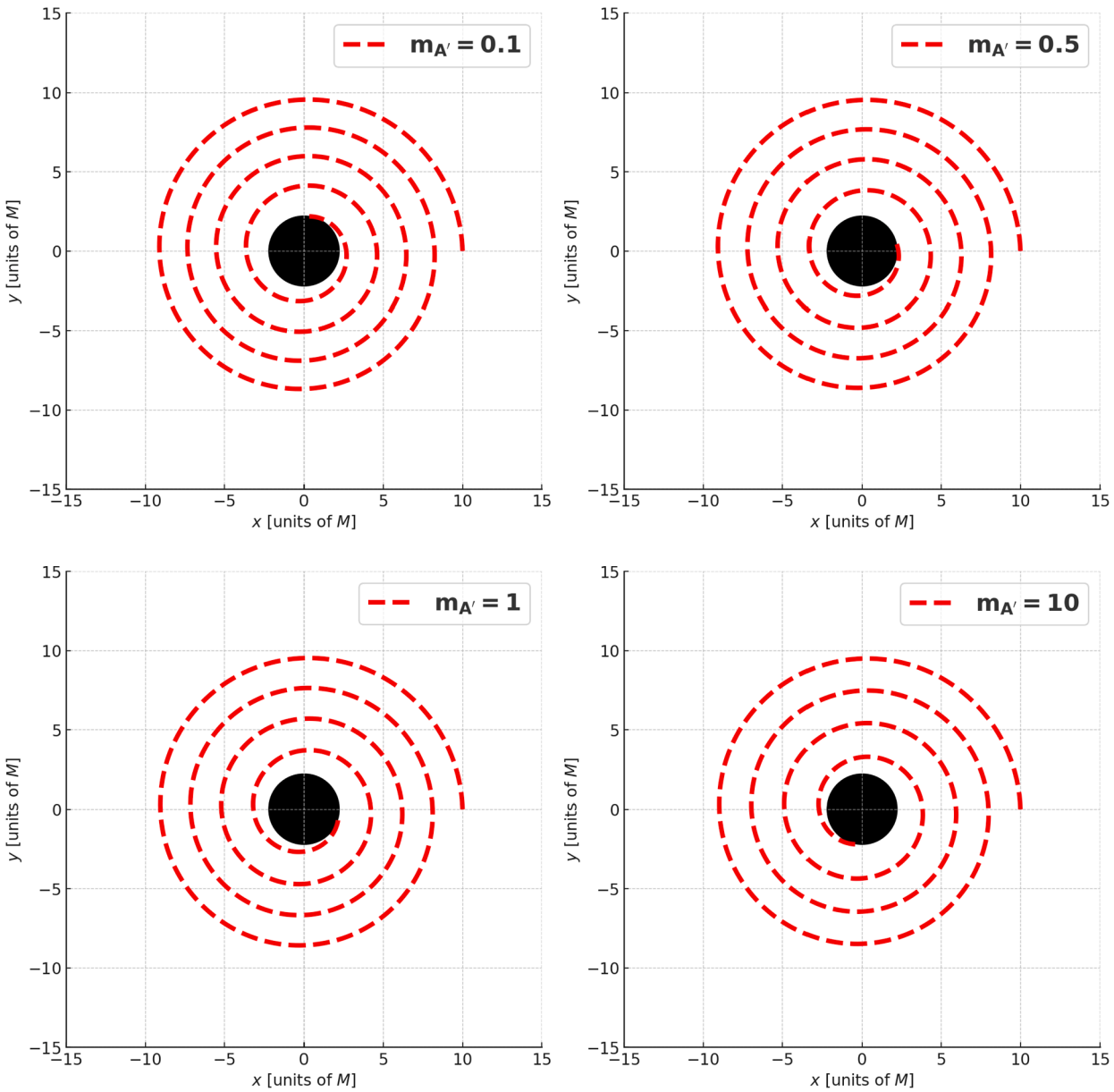

Fig. 21. The trajectories of the test particle of BH solutions in DPM for different values of $m_{A'}M$ for fixed $M = g_D = 0.5$, $\mu_f = S_{12} = 1$ and $\Lambda = 1.7$.

interaction. Fig. 25 provides a combined analysis of the simultaneous variation of $m_{A'}$ and g_D, confirming that while $m_{A'}$ increases orbital motion, g_D decreases it, and their interplay govern the radial profile of $\Omega(r)$. In Fig. 26, a comparative plot between the DPM and classical Schwarzschild and RN-like BHs reveal that the dark photon corrections yield orbital velocities distinct from standard general relativity, often deviating significantly near the horizon. The underlying modeling is based on the relation $\Omega^2 = \frac{1}{2r} f'(r)$, derived from the condition of circular motion, where $f(r)$ includes dark photon-induced exponential and spin-dipole terms. Physically, these findings suggest that the dark photon parameters not only influence the dynamics of orbiting matter but also modify the rotation profiles of accretion disks. The proper angular velocity is given by $\Omega(r) = \dot{\phi} = \frac{L}{r^2}$, which leads to

$$\omega = \frac{r}{2}\left(2f - rf'\right)\Omega(r), \tag{46}$$

$$\omega = \Omega(r)(e^{-m_{A'}r}(m_{A'}{}^2(g_D{}^2\Lambda^2 r^3 - rS_{12}\mu_f^2) + \Lambda^2 r(3g_D{}^2 + 4\pi e^{m_{A'}r}(r-3M))m_{A'}(3g_D{}^2\Lambda^2 r^2 - 4S_{12}\mu_f^2)))(4\pi\Lambda^2 r)^{-1}. \tag{47}$$

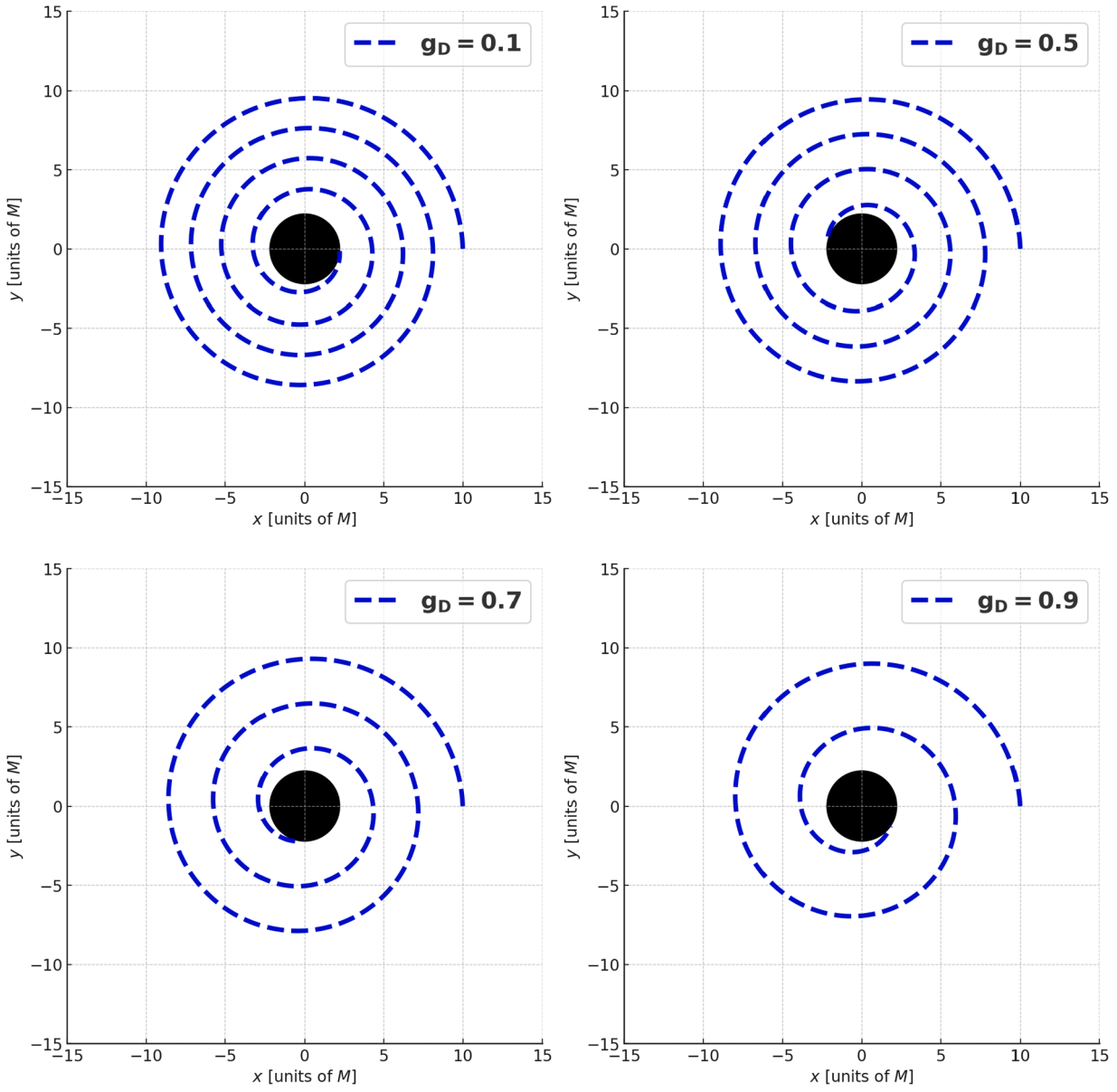

Fig. 22. The trajectories of the test particle of BH solutions in DPM for different values of g_D for fixed $M = m_{A'}M = 0.5$, $\mu_f = S_{12} = 1$ and $\Lambda = 1.7$.

To calculate the geodesic precession frequency $\Theta_{\rm GPF}$ of a gyroscope in orbit, we use Eq. (47) and apply the approach described in Ref.[25]. The resulting geodetic precession frequency is expressed as

$$\Theta_{\rm GPF} = \Omega - \Omega_{\rm GPF}, \quad \Omega_{\rm GPF} = \Omega\sqrt{f - \Omega^2 r^2}. \tag{48}$$

Substituting Eqs. (45) and (47) into Eq. (48), we derive the explicit expression for the geodetic precession frequency $\Theta_{\rm GPF}$ as [22]

$$\Theta_{\rm GPF} = \frac{rf'(r)}{2r}\left[1 - \frac{r}{\sqrt{2f - rf'(r)}}\right], \tag{49}$$

$$\begin{aligned}\Theta_{\rm GPF} = &\left(4\pi\Lambda^2 M r_c\, e^{m_{A'}r_c} + \Lambda^2 g_D^2 r_c(m_{A'}^2 r_c^2 + m_{A'}r_c + 1) - S_{12}m_{A'}\mu_f^2(m_{A'}r_c + 2)\right)^{1/2} e^{-\frac{7}{2}m_{A'}r_c}(2\pi^{5/2}\Lambda^2 r_c^3)^{-1} \\ &\times\left[\pi^2\Lambda r_c\, e^{3m_{A'}r_c} - (2)^{1/2}\pi^{3/2}\left(-\pi\Lambda^2 M r_c\, e^{m_{A'}r_c} + \tfrac{1}{6}\Lambda^2 g_D^2 r_c(m_{A'}r_c + 1) - \tfrac{1}{12}\Lambda^2 g_D^2 r_c(m_{A'}^2 r_c^2 + m_{A'}r_c + 1)\right.\right. \\ &\left.\left. + \tfrac{1}{3}\pi\Lambda^2 r_c^2\, e^{m_{A'}r_c} + \tfrac{1}{12}S_{12}m_{A'}\mu_f^2(m_{A'}r_c + 2) - \tfrac{1}{6}S_{12}m_{A'}\mu_f^2\right)^{1/2}\right]\end{aligned} \tag{50}$$

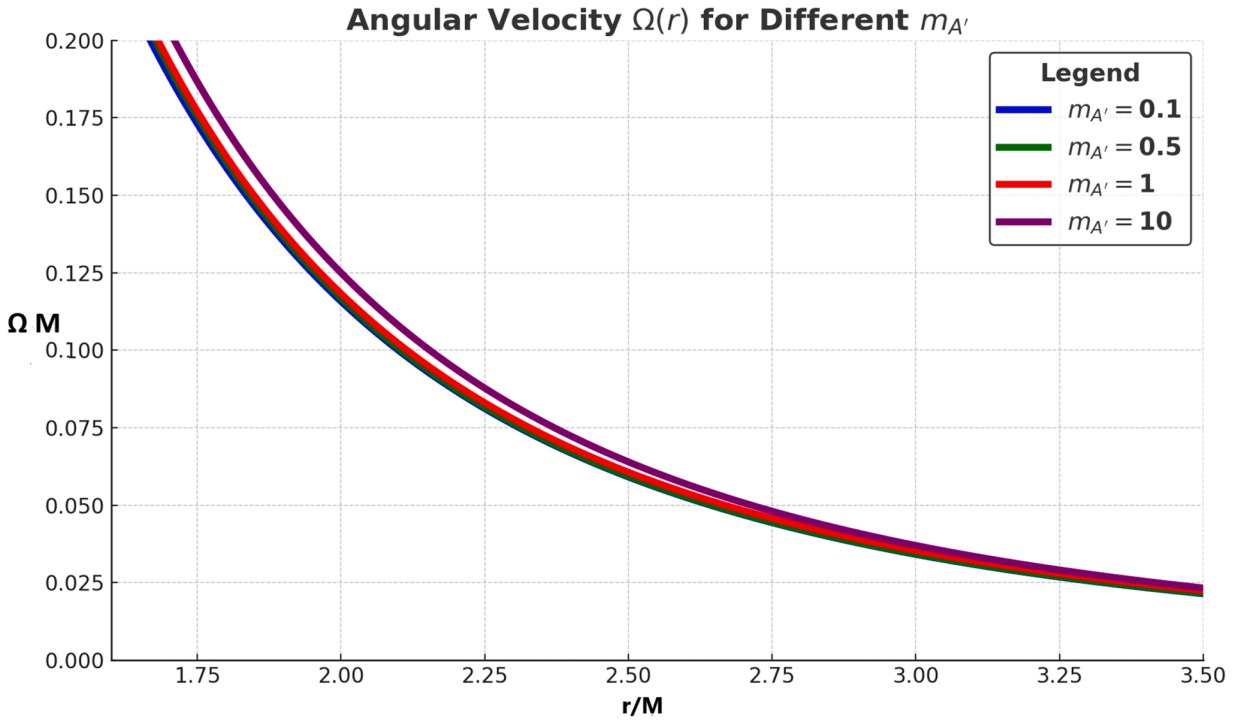

Fig. 23. The plot of orbital velocity $\Omega(r)M$ as a function of radial coordinate r/M for BH solutions in DPM for different values of $m_{A'}M$ for fixed $M = g_D = 0.5$, $\mu_f = S_{12} = 1$ and $\Lambda = 1.7$.

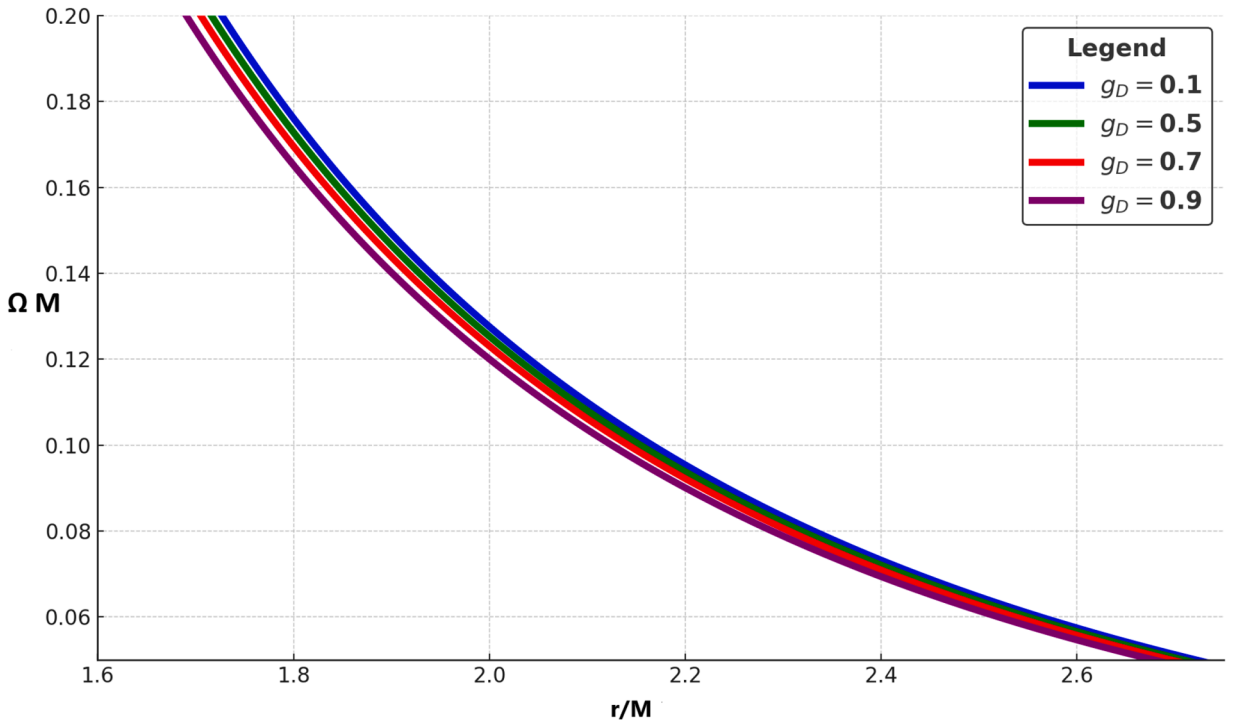

Fig. 24. The plot of orbital velocity $\Omega(r)M$ as a function of radial coordinate r/M for BH solutions in DPM for different values of g_D for fixed $M = m_{A'}M = 0.5$, $\mu_f = S_{12} = 1$ and $\Lambda = 1.7$.

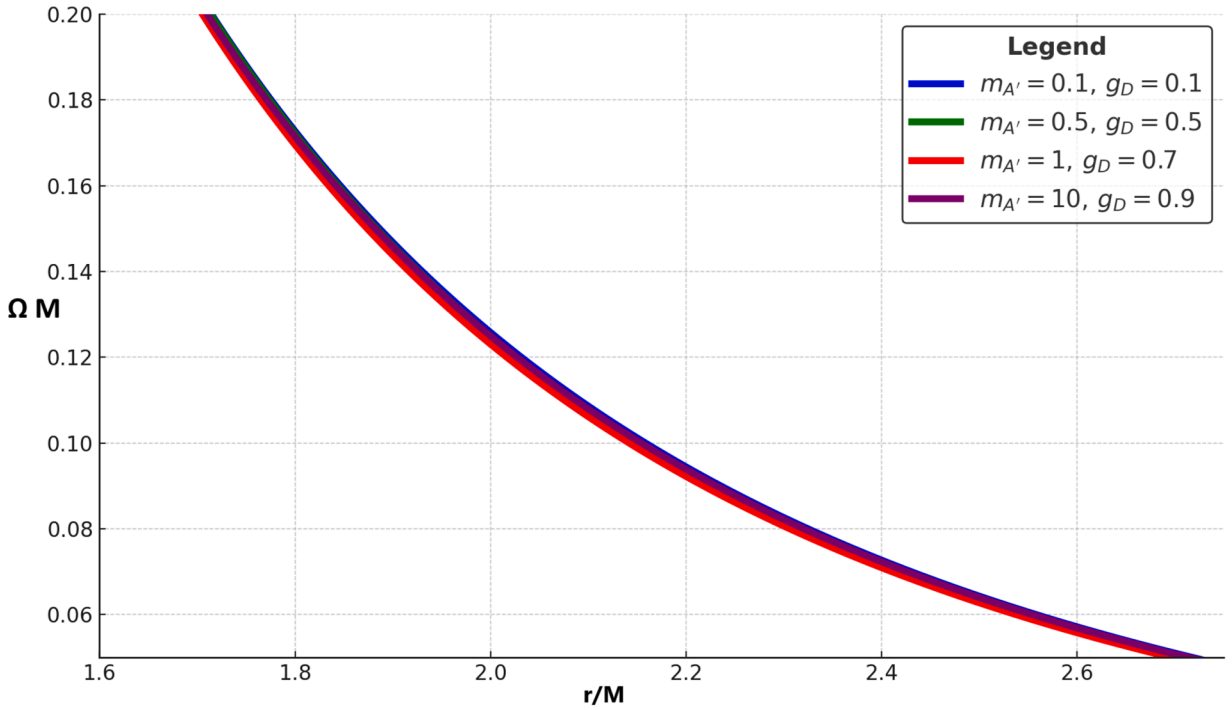

Fig. 25. The plot of orbital velocity $\Omega(r)M$ as a function of radial coordinate r/M for BH solutions in DPM for different values of $m_{A'}M$ and g_D for fixed $M = 0.5$, $\mu_f = S_{12} = 1$ and $\Lambda = 1.7$.

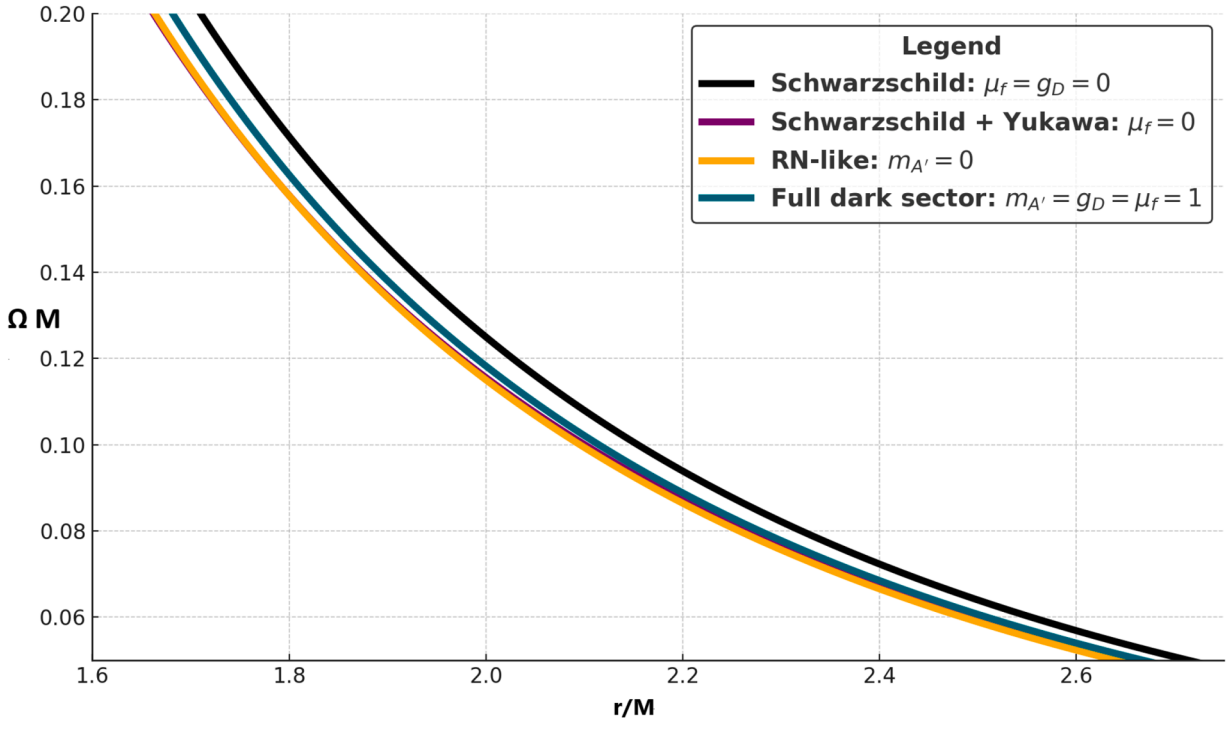

Fig. 26. The plot of orbital velocity $\Omega(r)M$ as a function of radial coordinate r/M for BH solutions in DPM, Schwarzschlid and RN-like BHs.

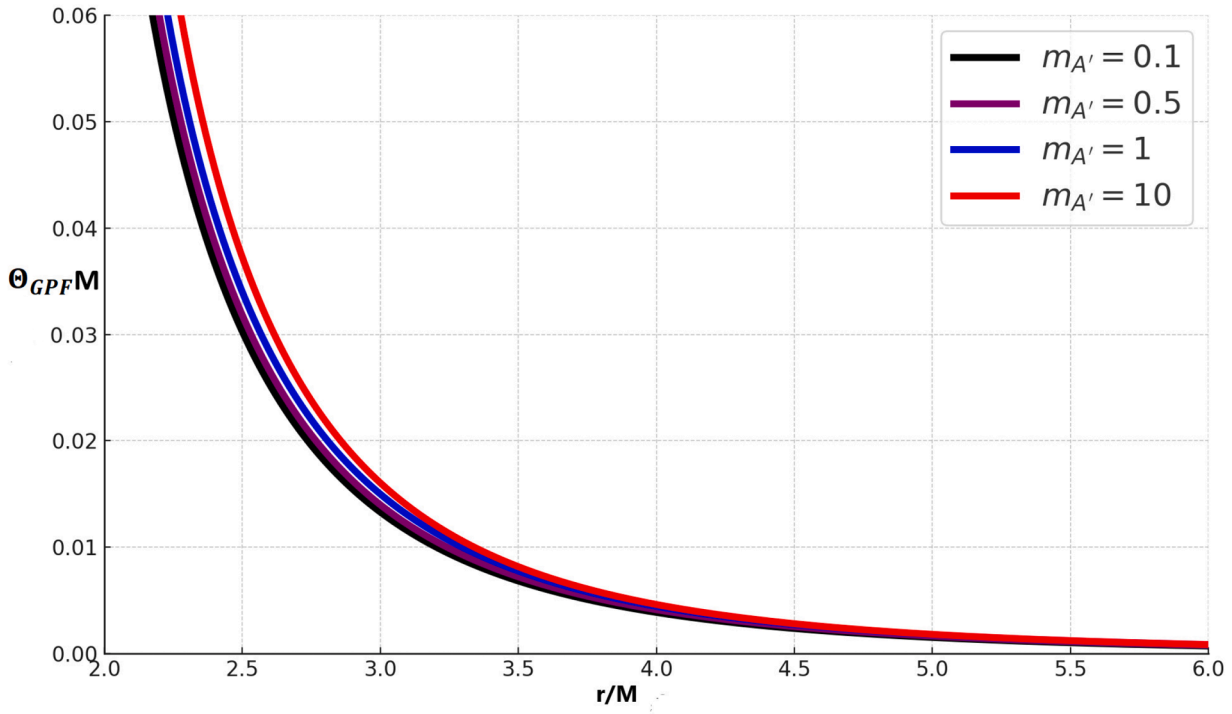

Fig. 27. The plot of geodetic precession frequency $\Theta_{\text{GPF}}M$ as a function of radial coordinate r/M for BH solutions in DPM for different values of $m_{A'}M$ for fixed $M = g_D = 0.5$, $\mu_f = S_{12} = 1$ and $\Lambda = 1.7$.

The expression in (50) clearly shows that several factors such as the dark gauge coupling g_D and the dark photon mass $m_{A'}$ have a significant impact on the geodesic precession frequency Θ_{GPF}. These influences highlight crucial deviations from the classical predictions of general relativity, arising from nonlinear and quantum effects in the vicinity of compact objects.

Figs. 27 to 30 display the behavior of the geodetic precession frequency Θ_{GPF} as a function of the radial coordinate r for solutions in DPM, examining the effects of dark photon mass $m_{A'}$ and dark gauge coupling g_D, along with a comparative analysis with Schwarzschild and RN-like geometries. In Fig. 27, increasing $m_{A'}$ leads to a noticeable increase of Θ_{GPF}, especially near the , indicating that heavier dark photons increase the spacetime curvature-induced precession experienced by a gyroscope in circular orbit. This results from the exponential suppression in the metric function $f(r)$, which weakens the spacetime dragging effect. In contrast, Fig. 28 shows that higher values of g_D weakers Θ_{GPF} across all radii, suggesting a lower influence of the dark photon field on the geometry and the resulting precession frequency. Fig. 29 combines both parameters, revealing that while $m_{A'}$ amplify the effect, g_D lower it. Fig. 30 compares the DPM with Schwarzschild and RN-like solutions, demonstrating that the inclusion of dark sector corrections results in a steeper rise in Θ_{GPF} near the event horizon, significantly deviating from general relativity predictions. Physically, these results imply that the precession of gyroscopes or orbiting bodies is highly sensitive to the presence of dark photon fields, affecting relativistic frame-dragging and potentially observable through precision measurements of orbital dynamics. Finally, our goal is to find the orbital speed of a time-like particle moving around the BH at a distance much greater than the event horizon. This scenario is similar to a distant star orbiting the central BH within a galaxy. To a first approximation, the lapse function $f(r)$ can be expressed as follows

$$f(r) = 1 + 2\Phi(r), \tag{51}$$

where $\Phi(r)$ represents the Newtonian gravitational potential acting on a time-like particle with unit mass. By employing the metric function from Eq. (14), we explicitly derive the gravitational potential $\Phi(r)$ as

$$\Phi(r) = \frac{1}{2}\left(-\frac{2M}{r} + \frac{g_D^2}{2\pi r}e^{-m_{A'}r}(m_{A'}r + 1) - \frac{\mu_f^2 S_{12} m_{A'} e^{-m_{A'}r}}{2\pi\Lambda^2 r^2}\right). \tag{52}$$

This formula represents the modified Newtonian potential that accounts for the influence of the dark gauge coupling g_D and the dark photon mass $m_{A'}$ .It offers an approximate yet valuable perspective on the orbital dynamics of massive particles, such as stars, at galactic scales, emphasizing the deviations from classical Newtonian gravity caused by fundamental field interactions. The effective gravitational force experienced by a time-like particle in a circular orbit is given by the following expression

$$F_c = -\frac{\partial\Phi(r)}{\partial r}, \tag{53}$$

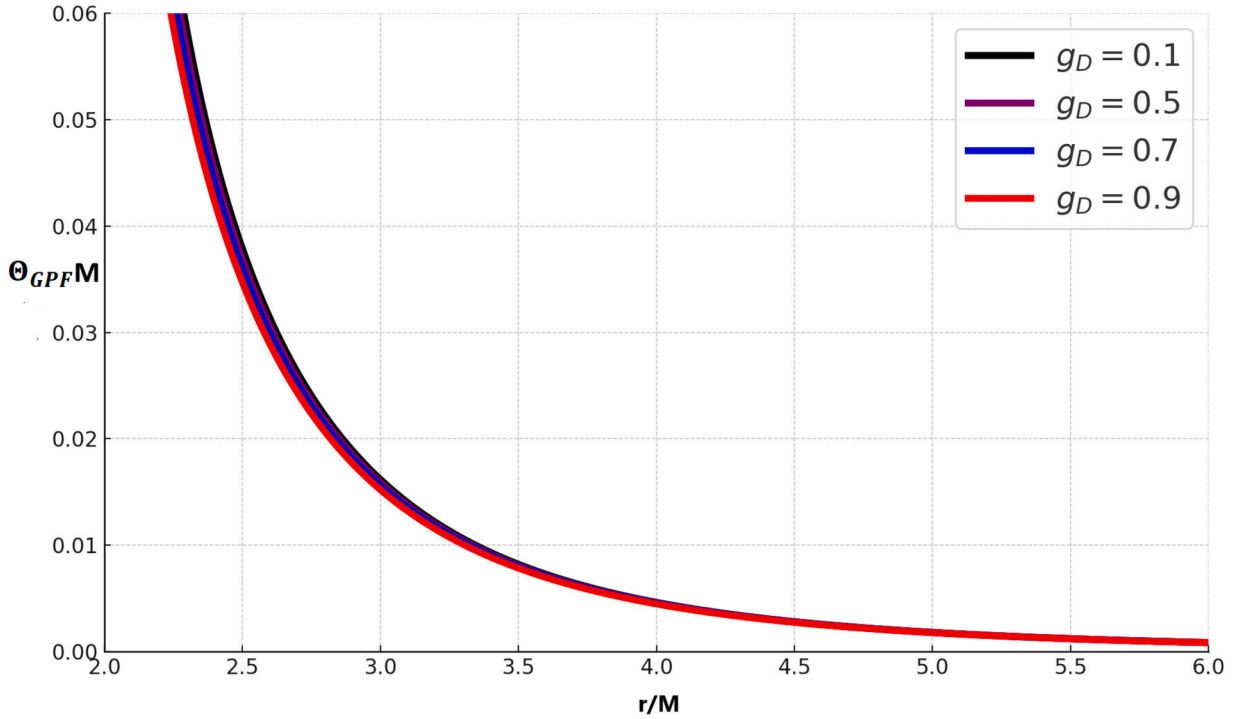

Fig. 28. The plot of geodetic precession frequency $\Theta_{\mathrm{GPF}} M$ as a function of radial coordinate r/M for BH solutions in DPM for different values of g_D for fixed $M = m_{A'} M = 0.5$, $\mu_f = S_{12} = 1$ and $\Lambda = 1.7$.

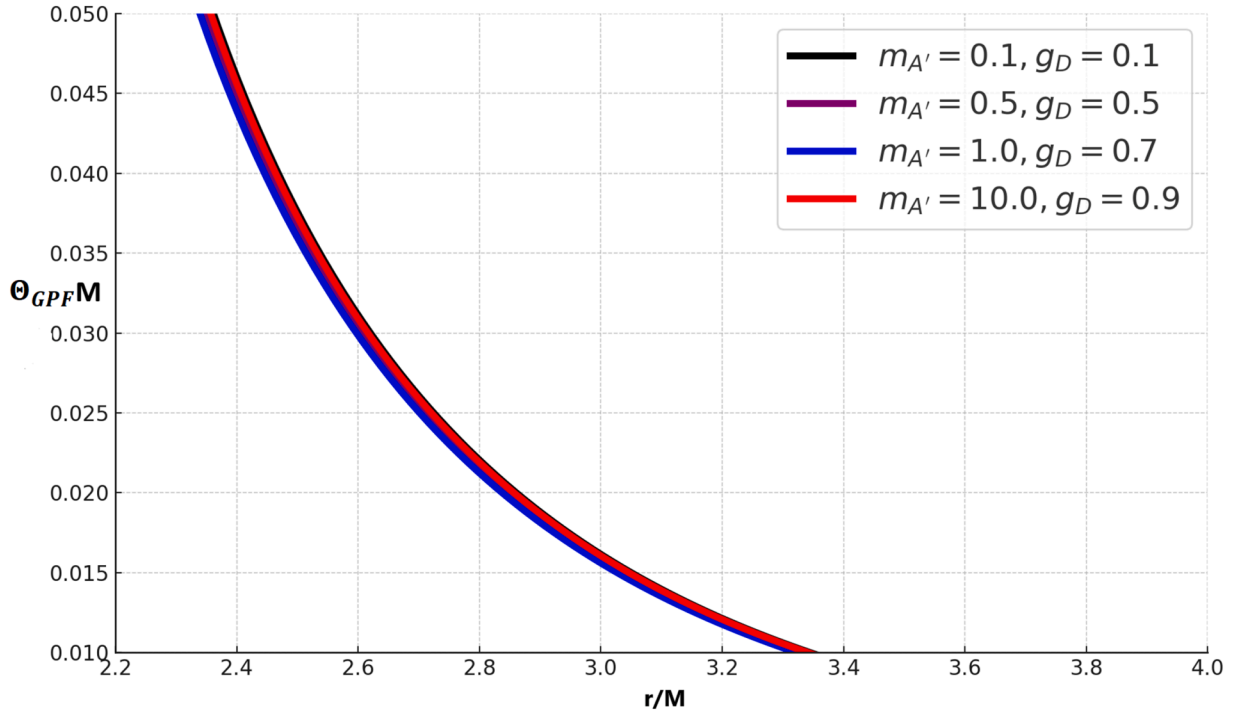

Fig. 29. The plot of geodetic precession frequency $\Theta_{\mathrm{GPF}} M$ as a function of radial coordinate r/M for BH solutions in DPM for different values of $m_{A'} M$ and g_D for fixed $M = 0.5$, $\mu_f = S_{12} = 1$ and $\Lambda = 1.7$.

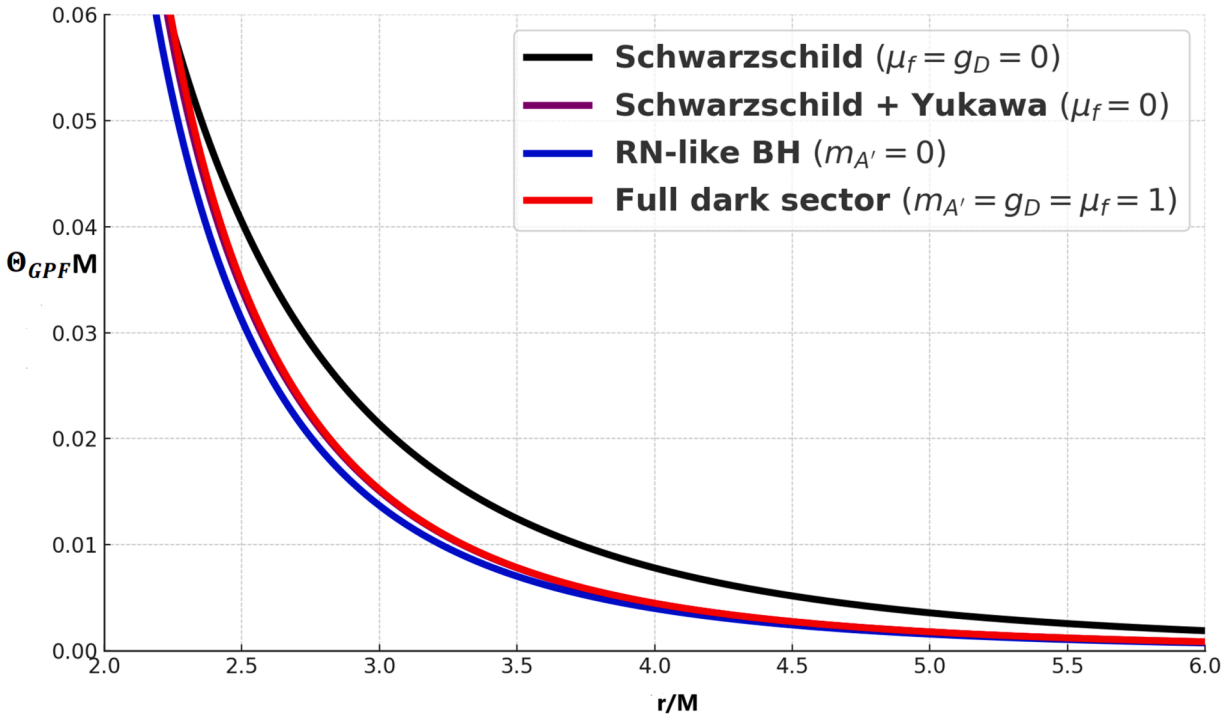

Fig. 30. The plot of geodetic precession frequency $\Theta_{\mathrm{GPF}}M$ as a function of radial coordinate r/M for BH solutions in DPM, Schwarzschlid and RN-like BHs.

By applying the potential given in Eq. (52), we directly obtain

$$F_c(r) = \frac{M}{r^2} - \frac{g_D^2}{4\pi}\left[\frac{1}{r^2}e^{-m_{A'}r}(m_{A'}r+1) + m_{A'}^2 e^{-m_{A'}r}\right] + \frac{\mu_f^2 S_{12} m_{A'} e^{-m_{A'}r}}{4\pi\Lambda^2}\left(\frac{2}{r^3} + \frac{m_{A'}}{r^2}\right).$$

This central force F_c corresponds to the centripetal acceleration $v(r)^2/r$, where $v(r)$ represents the velocity of a time-like particle moving in a circular orbit. From this relationship, we derive the following formula for the orbital speed in a circular path

$$v(r) = \sqrt{r|F_c|}, \tag{54}$$

$$v(r) = \sqrt{r\left|\frac{M}{r^2} - \frac{g_D^2}{4\pi}\left[\frac{1}{r^2}e^{-m_{A'}r}(m_{A'}r+1) + m_{A'}^2 e^{-m_{A'}r}\right] + \frac{\mu_f^2 S_{12} m_{A'} e^{-m_{A'}r}}{4\pi\Lambda^2}\left(\frac{2}{r^3} + \frac{m_{A'}}{r^2}\right)\right|}.$$

The expression (54) indicates that the circular velocity of time-like particles in orbit is notably shaped by various parameters, including the dark gauge coupling g_D and the dark photon mass $m_{A'}$. These parameters alter the gravitational interaction, leading to departures from classical orbital behavior, especially at large radial distances. Such deviations play a key role in investigating astrophysical phenomena, such as the motion of stars around galactic and the evaluation of alternative gravitational theories.

Figs. 31 to 34 illustrate the variation of the circular orbital speed $v(r)$ of time-like particles as a function of radial coordinate r for BHs in DPM, examining the influence of dark photon mass $m_{A'}$ and dark gauge coupling g_D. In Fig. 31, increasing $m_{A'}$ leads to a increase in $v(r)$ at smaller radii, with the peak of the orbital speed curve shifting outward. This indicates that heavier dark photons significantly effects the gravitational binding near the due to stronger Yukawa-type screening, resulting in lower orbital velocities and more distant stable orbits. Fig. 32 shows that as g_D increases, the orbital speed profile becomes steeper with lower peak values near the horizon, reflecting weak gravitational attraction from stronger gauge coupling. Fig. 33 analyzes the combined impact of $m_{A'}$ and g_D, confirming their competing effects: $m_{A'}$ acts to flatten and spread the velocity curve, while g_D steepens it and pulls the maximum closer to the BH. Fig. 34 provides a comparison with classical Schwarzschild and RN-like BHs, demonstrating that the DPM produces distinct orbital velocity behaviors, particularly higher velocities near the event horizon, which are absent in standard GR spacetimes. Physically, such changes in orbital velocity influence the structure and emissivity of accretion disks, rotational curves of stars near galactic centers, and relativistic precession rates.

The analysis of geodesic motion has revealed how dark photon parameters significantly alter the dynamics of both massless and massive particles, influencing orbital stability, ISCO behavior, and photon sphere characteristics. These results serve as a crucial foundation for understanding the observable consequences of such modifications, since the structure of photon orbits directly govern the BHs optical appearance to distant observers. In particular, the deformation of the photon sphere induced by Yukawa screening

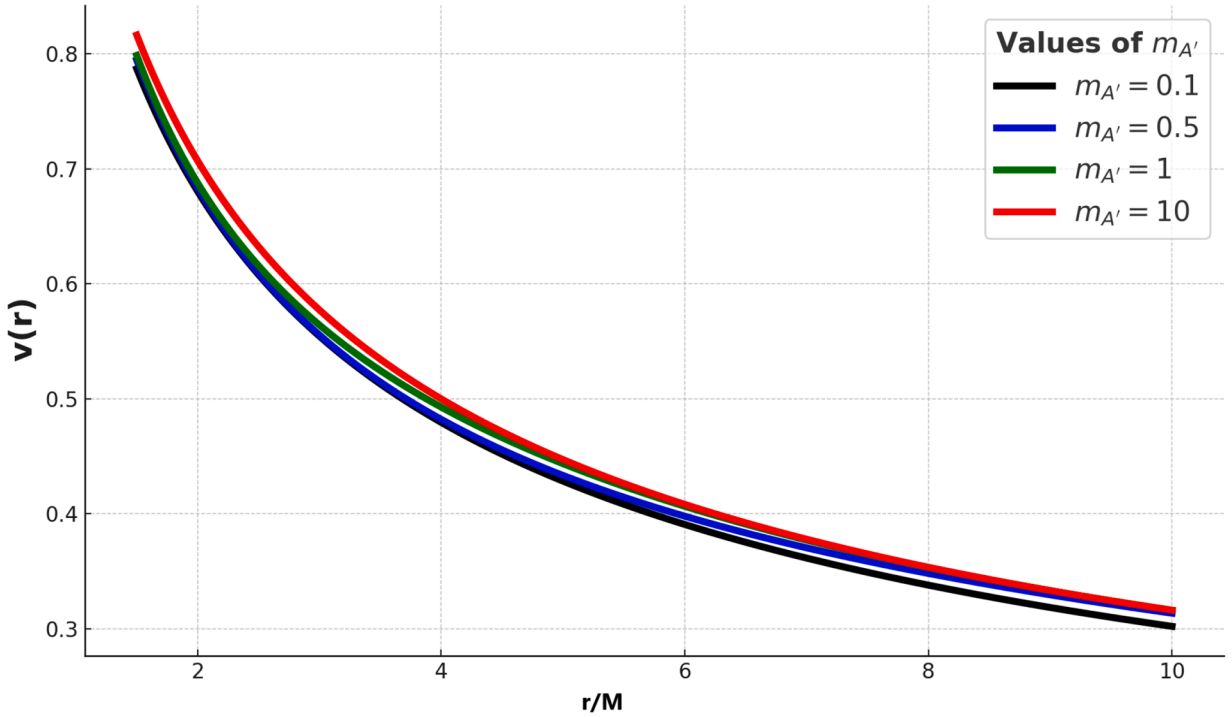

Fig. 31. The plot of circular orbital speed $v(r)$ as a function of radial coordinate r/M for BH solutions in DPMs for different values of $m_{A'}M$ for fixed $M = g_D = 0.5$, $\mu_f = S_{12} = 1$ and $\Lambda = 1.7$.

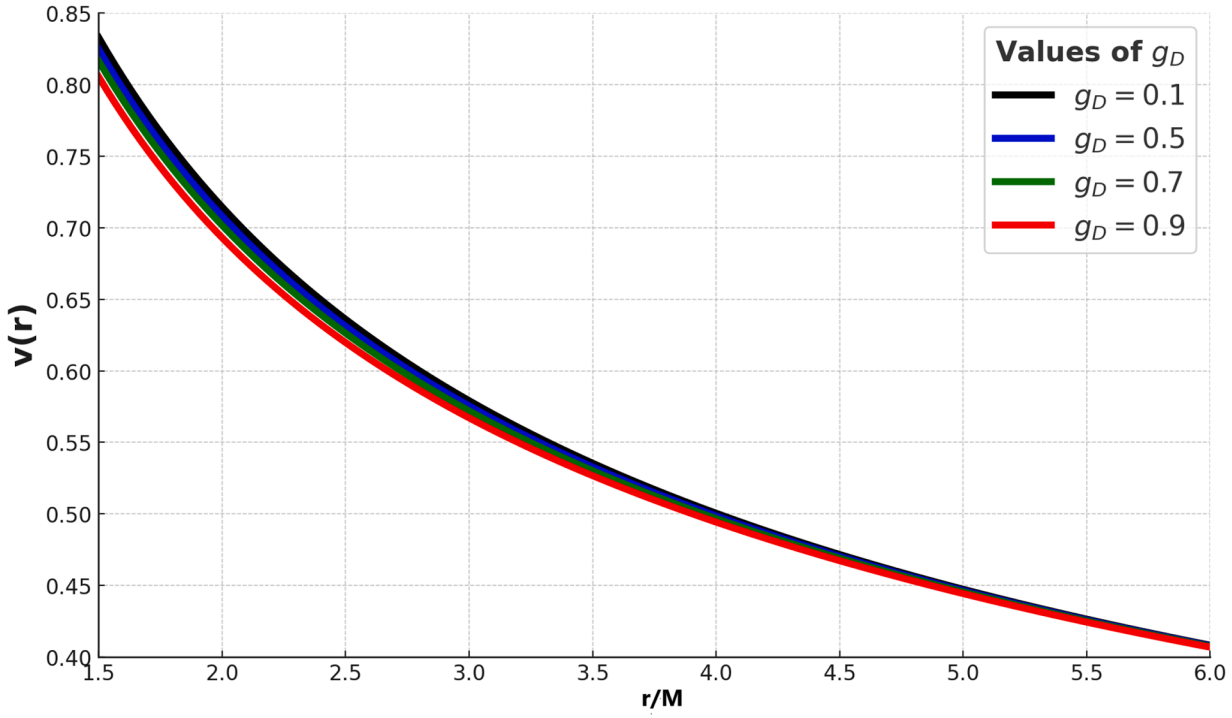

Fig. 32. The plot of circular orbital speed $v(r)$ as a function of radial coordinate r/M for BH solutions in DPMs for different values of g_D for fixed $M = m_{A'}M = 0.5$, $\mu_f = S_{12} = 1$ and $\Lambda = 1.7$.

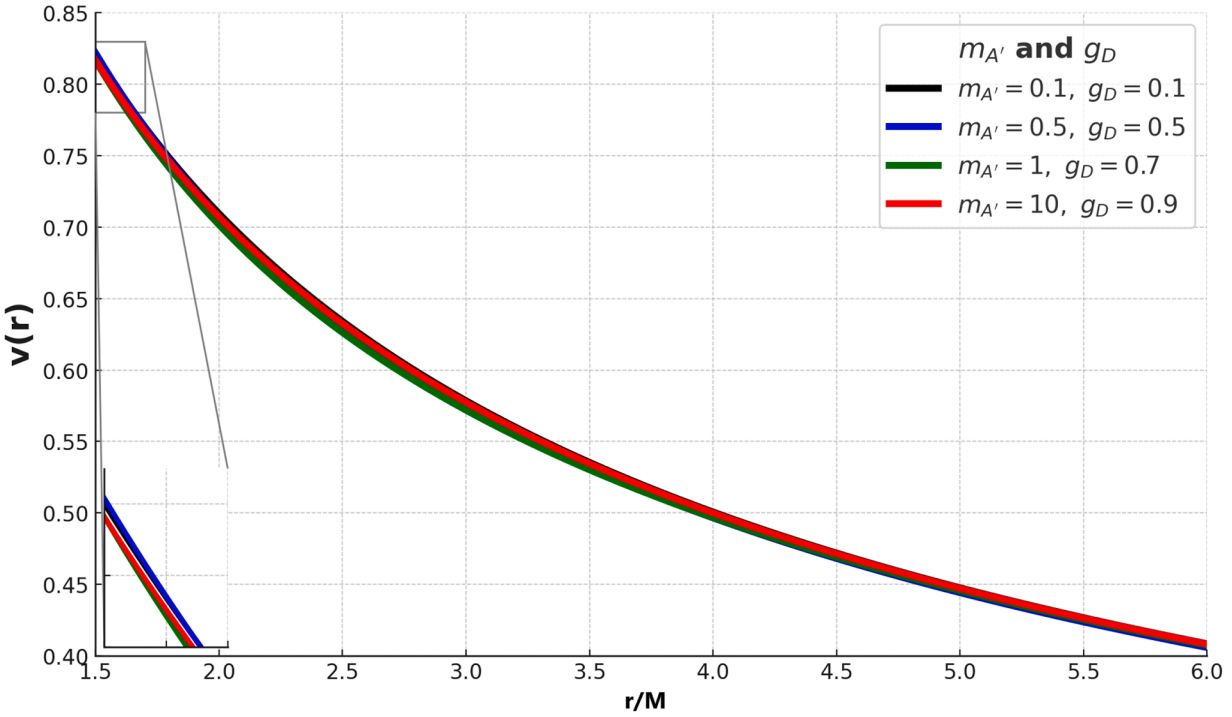

Fig. 33. The plot of circular orbital speed $v(r)$ as a function of radial coordinate r/M for BH solutions in DPMs for different values of $m_{A'}M$ and g_D for fixed $M = 0.5$, $\mu_f = S_{12} = 1$ and $\Lambda = 1.7$.

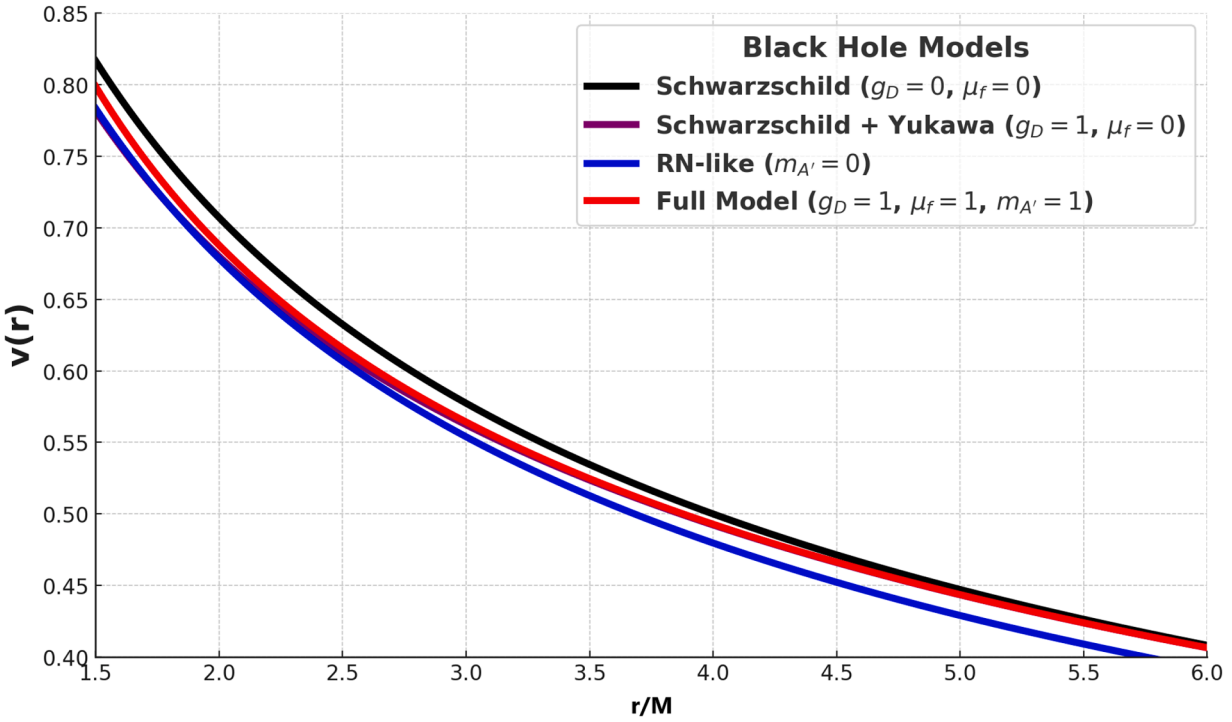

Fig. 34. The plot of circular orbital speed $v(r)$ as a function of radial coordinate r/M for BH solutions in DPMs, Schwarzschlid and RN-like BHs.

Table 4
Photon sphere radius $r_{\rm ph}/M$ for different values of $m_{A'}M$ and g_D in the DPM.

$m_{A'}M$	$g_D = 0.1$	$g_D = 0.5$	$g_D = 0.7$	$g_D = 0.9$
0.1	3.05127	3.10259	3.15348	3.20471
0.5	3.00312	3.05486	3.10632	3.15790
1	2.95674	3.00824	3.05978	3.11119
10	2.80345	2.85498	2.90627	2.95713

and gauge coupling effects manifests in the size and shape of the BH shadow. Therefore, having established the geodesic framework, we now turn to the study of optical properties and shadow images, which provide one of the most direct and measurable astrophysical signatures of dark photon corrections.

4. Optical properties and shadows of black hole solutions in dark photon models

4.1. Analysis of photon sphere radius

The study of shadows has emerged as a powerful observational tool to probe the nature of spacetime geometry and the influence of additional fields beyond general relativity. The presence of dark photon fields modifies the effective metric around the BH, thereby altering the photon sphere structure and subsequently affecting the shadow cast against a backdrop of luminous matter. In this section, we focus on analyzing the shadow radius and optical appearance of solutions in DPM, incorporating both Yukawa-type and magnetic dipole corrections. By determining the photon sphere radius and employing celestial coordinates, we explore how parameters such as the dark gauge coupling g_D and dark photon mass $m_{A'}$ reshape the shadow contour. Several methods have been suggested for calculating the shadow radius of a spherically symmetric , as reviewed in Ref. [26]. One commonly adopted approach is to determine the photon sphere radius $r_{\rm ph}$ using the condition

$$rD'(r) = D(r), \tag{55}$$

where $D(r) = \sqrt{f(r)}$ with $f(r)$ representing the lapse function of a static, spherically symmetric spacetime. However, the equation's highly nonlinear character makes an analytical solution intractable. The numerically evaluated photon sphere radii for various values of g_D and $m_{A'}$ are presented in Table 4.

4.2. Analysis of shadow radius

The shadow radius R_s , as seen by a static observer at spatial infinity, is determined using the photon sphere radius $r_{\rm ph}$ and is expressed as

$$R_s = \frac{r_{\rm ph}}{\sqrt{f(r_{\rm ph})}}, \tag{56}$$

where $f(r)$ is the lapse function of the spacetime, defined in Eq. (11). Due to the complexity of the metric function and the implicit dependence of $r_{\rm ph}$ on various parameters, an analytical expression for R_s is not feasible. Therefore, Eq. (11) is evaluated numerically for different values of the magnetic monopole.

Figs. 35 and 36 present the dependence of the photon sphere radius $r_{\rm ph}$ and the corresponding shadow radius R_s on the dark photon mass $m_{A'}$ and dark gauge coupling g_D in the context of dark photon-modified spacetimes. As shown in Fig. 35, increasing $m_{A'}$ results in a monotonic decrease in $r_{\rm ph}$ for fixed values of g_D, indicating that a more massive dark photon compresses the photon sphere inward due to stronger exponential suppression in the modified metric function $f(r)$. In contrast, higher values of g_D cause $r_{\rm ph}$ to increase, which reflects the enhanced effective gravitational pull stemming from stronger gauge coupling. Fig. 36 shows the corresponding shadow radius $R_s = r_{\rm ph}/\sqrt{f(r_{\rm ph})}$, and a similar trend is observed: larger $m_{A'}$ values reduce R_s, while increasing g_D expands it. These results demonstrate that the dark photon field significantly alters the optical geometry of the by modifying the spacetime curvature and thus the bending of light rays. The mathematical modeling highlights how Yukawa-type and magnetic dipole corrections enter the lapse function $f(r)$ and influence the photon sphere structure and the projected silhouette. Physically, these changes imply that the apparent size of the BH as seen by a distant observer can vary substantially from general relativity predictions, depending on the values of $m_{A'}$ and g_D. The numerically computed shadow radius values are summarized in Table 5, corresponding to different combinations of g_D and $m_{A'}$.

To represent the actual shadow of the BH as seen by a distant observer, we introduce the celestial coordinates (X, Y), which describe the apparent position of photons on the observer's sky. These coordinates are defined as

$$X = \lim_{r_o\to\infty}\left(-r_o^2 \sin\theta_o \frac{d\phi}{dr}\right), \tag{57}$$

$$Y = \lim_{r_o\to\infty}\left(r_o^2 \frac{d\theta}{dr}\right), \tag{58}$$

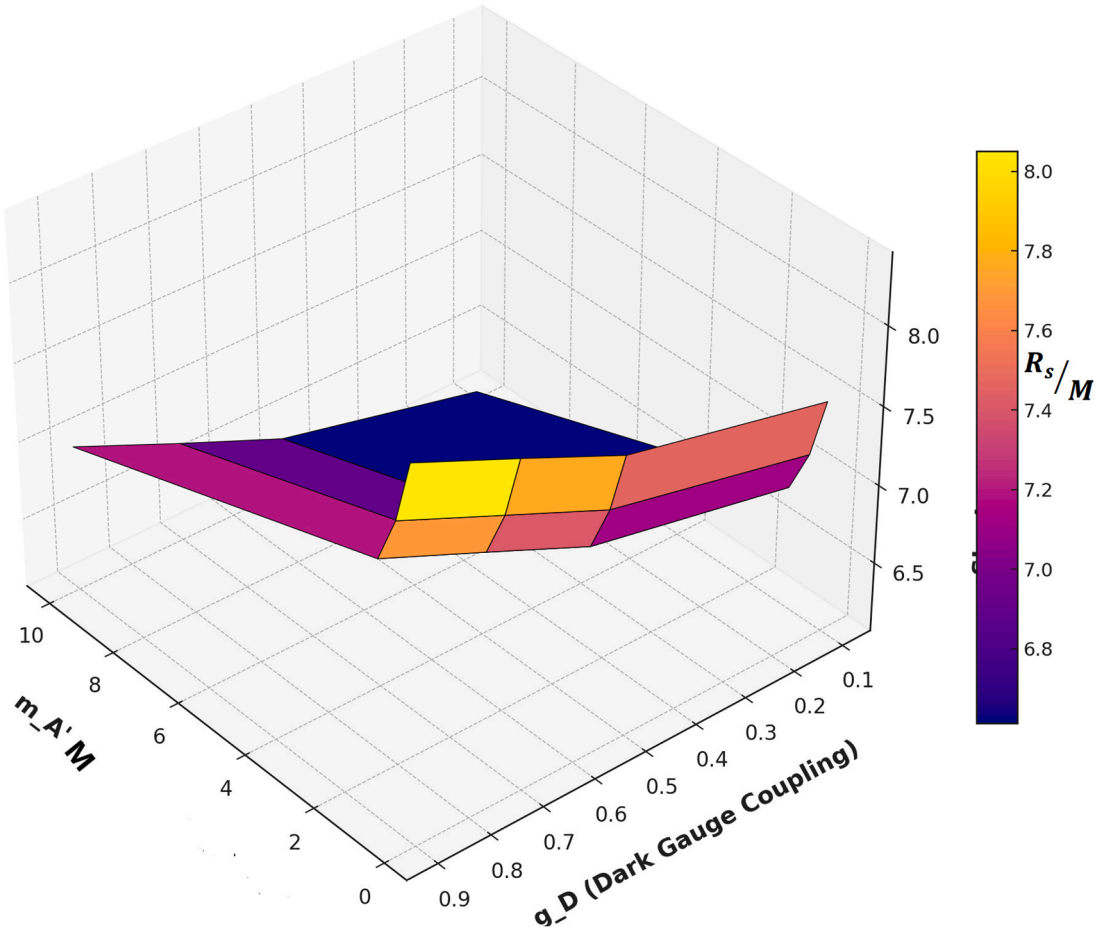

Fig. 35. The plot of photon sphere radius $r_{\rm ph}/M$ versus dark photon mass $m_{A'}M$ and dark gauge coupling g_D.

Table 5
Numerical results for the shadow radius R_s/M in DPM with Higher-Order Corrections. The radius decreases with increasing $m_{A'}M$ and increases with increasing g_D.

$m_{A'}M$	$g_D = 0.1$	$g_D = 0.5$	$g_D = 0.7$	$g_D = 0.9$
0.1	7.51342	7.80934	8.10725	8.39873
0.5	7.11856	7.41297	7.70385	7.99542
1	6.83211	7.10478	7.39890	7.68901
10	6.10439	6.40922	6.69288	6.98673

where r_o is the radial coordinate of the observer, and θ_o is the inclination angle. For a static observer at a large distance $r_o \to \infty$, in the equatorial plane $\theta_o = \pi/2$, the celestial coordinates simplify to the relation

$$X^2 + Y^2 = R_s^2. \tag{59}$$

This expression indicates that the shadow, when viewed on the celestial plane, takes the form of a circular disk with radius R_s, determined by the behavior of the photon sphere and the underlying spacetime geometry.

Figs. 37 and 38 depict the shadow images of BHs in DPMs for varying values of dark photon mass $m_{A'}$ and dark gauge coupling g_D, respectively, highlighting how these parameters influence the apparent shape and size of the shadow. In Fig. 37, increasing $m_{A'}$ leads to a noticeable contraction of the shadow radius, resulting in a smaller and more compact circular silhouette. This occurs due to the exponential Yukawa suppression in the metric function $f(r)$, which pulls the photon sphere inward and reduces the gravitational lensing strength near the BH. Conversely, Fig. 38 shows that increasing g_D causes the shadow to expand, with the boundary shifting outward, a direct consequence of the stronger gauge-induced curvature enhancing light deflection. These images are computed using the celestial coordinates (X, Y) derived from the geodesic equations and the condition $X^2 + Y^2 = R_s^2$, where R_s is the shadow

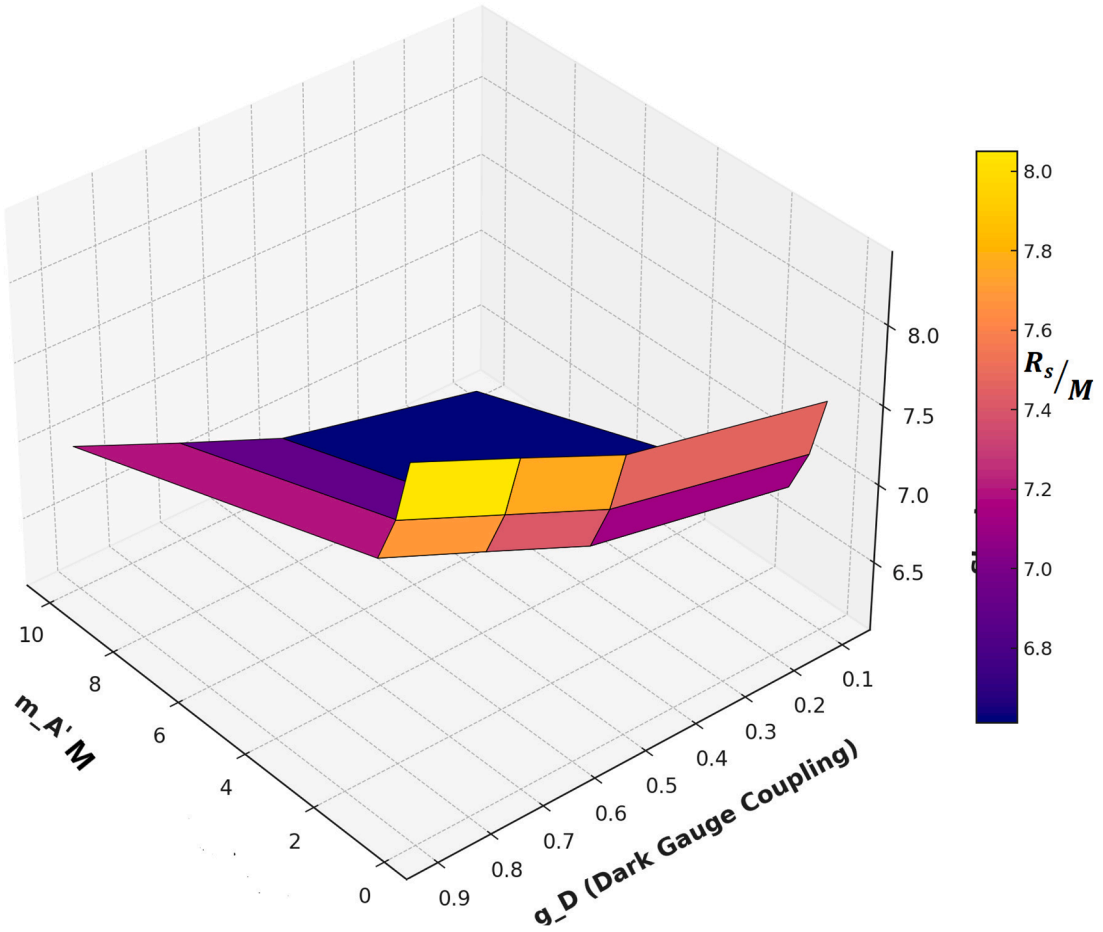

Fig. 36. The plot of shadow radius R_s/M versus dark photon mass $m_{A'}M$ and dark gauge coupling g_D.

radius. The key physical implication of these results is that the shadow size is not fixed, as in classical Schwarzschild spacetime, but dynamically depends on dark sector interactions. Such deviations can lead to observable changes in the morphology of shadows, potentially allowing the extraction of constraints on $m_{A'}$ and g_D from observational data.

The study of optical properties and shadow formation has shown that dark photon corrections leave distinctive imprints on the observable geometry of BHs, with shadow size and morphology sensitively dependent on the gauge coupling and dark photon mass. While these effects provide a direct observational window into the dark sector through imaging techniques, an equally important avenue lies in understanding how such corrections influence the interaction of BHs with surrounding fields. In particular, wave dynamics in the modified spacetime may give rise to amplification mechanisms beyond classical expectations. To further explore this connection between hidden sector physics and BH stability, we now turn our attention to the phenomenon of superradiance, where scalar field perturbations in the dark photon background can lead to wave amplification and energy extraction from the BH.

5. Superradiance phenomenon of black hole solutions in dark photon models

The phenomenon of superradiance provides energy extraction mechanisms from compact objects and serves as a sensitive probe for new physics beyond the Standard Model. When dark photon fields are present, the interaction between these vector fields and charged scalar perturbations leads to novel superradiant effects that can significantly influence the evolution and stability of BHs. In this section, we explore the superradiant scattering of scalar fields in the background of solutions modified by dark photon corrections. By solving the charged Klein-Gordon equation in curved spacetime, we derive the effective potential and identify the conditions under which wave amplification occurs. Furthermore, we examine the associated amplification factor and energy fluxes, highlighting the critical roles played by the dark gauge coupling g_D, dark photon mass $m_{A'}$, and the BH's horizon structure. This analysis reveals how the presence of dark sector interactions can enhance or suppress superradiance, potentially leading to observable astrophysical consequences and constraints on dark photon properties. In a curved spacetime, a massless scalar field $\phi(t, r, \theta, \varphi)$ minimally coupled

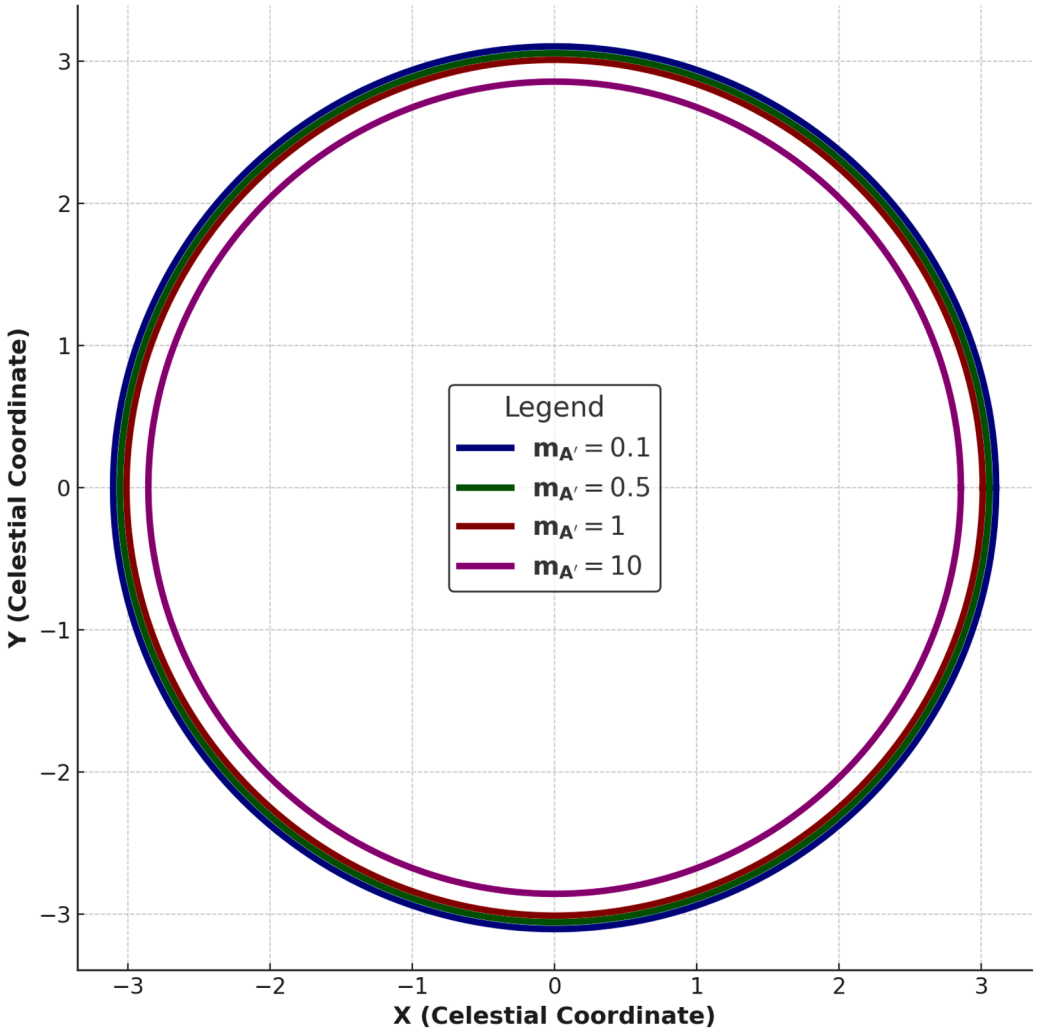

Fig. 37. The plot of shadows images of BH solutions in DPM for different values of $m_{A'}M$ for fixed $M = g_D = 0.5$, $\mu_f = S_{12} = 1$ and $\Lambda = 1.7$.

to a vector potential A_μ, is govern by the Klein-Gordon equation [27]

$$(\nabla^\mu - iQA^\mu)(\nabla_\mu - iQA_\mu)\phi = 0, \tag{60}$$

where Q is the charge of the scalar field. In the static, spherically symmetric spacetime given by Eq. (1), we decompose the field as follows

$$\phi(t, r, \theta, \varphi) = e^{-i\omega t} R(r) Y(\theta, \varphi), \tag{61}$$

where $Y(\theta, \varphi)$ are the spherical harmonics and ω is the frequency of the scalar field. Inserting Eq. (61) into Eq. (60), we derive the radial equation for $R(r)$

$$\frac{d^2R(r)}{dr^2} + \left(\frac{f'}{f} + \frac{2}{r}\right)\frac{dR(r)}{dr} + \left[\frac{\omega^2}{f^2} - \frac{l(l+1)}{r^2 f} - \frac{2\omega Q}{rf^2} + \frac{Q^2}{r^2 f^2}\right]R(r) = 0, \tag{62}$$

where $l = 0, 1, 2, \ldots$ is the spherical harmonic index, and $f(r)$ is the lapse function. To simplify the analysis further, we define the tortoise coordinate r_* as

$$r_* = \int \frac{dr}{f(r)}, \qquad u(r) = rR(r), \tag{63}$$

such that the radial equation takes the form of a Schrdinger-like equation

$$\frac{d^2u(r)}{dr_*^2} + V_{\text{eff}}(r)u(r) = 0. \tag{64}$$

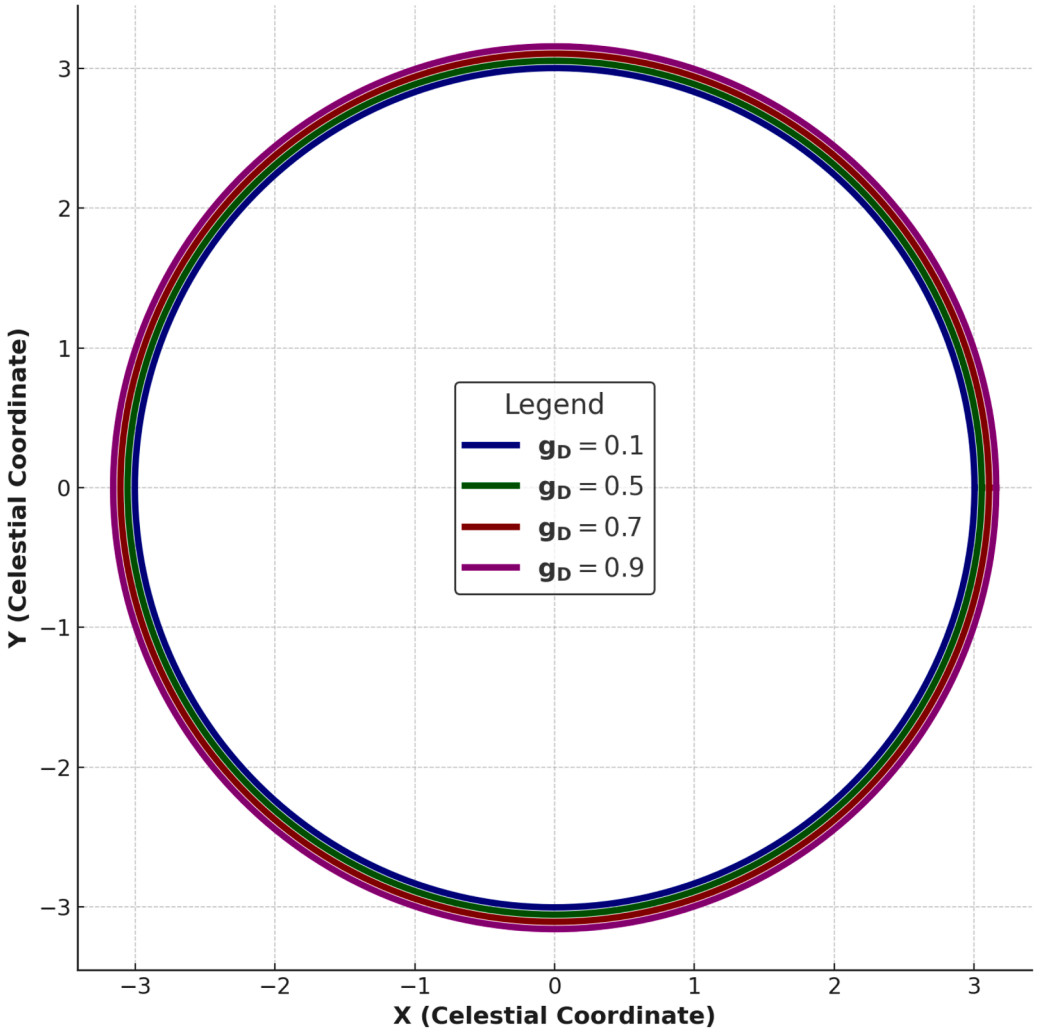

Fig. 38. The plot of shadows images of BH solutions in DPM for different values of g_D for fixed $M = m_{A'} M = 0.5$, $\mu_f = S_{12} = 1$ and $\Lambda = 1.7$.

Here, $u(r)$ is the rescaled radial function, and $V_{\text{eff}}(r)$ is the effective potential, encapsulating the influence of the geometry, scalar field charge Q and the angular momentum l. This framework is crucial for studying the phenomenon of superradiance, incident scalar waves can be amplified upon scattering off the BH. The effective potential $V_{\text{eff}}(r)$, which encodes the curvature of the background spacetime and the properties of the test scalar field, is given by [28]

$$V_{\text{eff}}(r) = \omega^2 - \left(\frac{f f'}{r} + \frac{l(l+1)f}{r^2} + \frac{2\omega Q}{r} - \frac{Q^2}{r^2} \right). \tag{65}$$

From Eq. (64), it is evident that the behavior of the radial function $u(r)$ is govern by the sign of $V_{\text{eff}}(r)$. In the region where $V_{\text{eff}}(r) > 0$, the solution $u(r)$ is oscillatory, corresponding to propagating wave modes. In the region where $V_{\text{eff}}(r) < 0$, the solution becomes exponential either growing or decaying which is the region where superradiance occurs. As the angular momentum quantum number l increases, the height of the potential barrier decreases. Conversely, oppositely charged particles are attracted more strongly. Importantly, the effective potential $V_{\text{eff}}(r)$ does not explicitly depend on the coupling constant of the modified gravity theory. Instead, the coupling constant indirectly affects the potential through its impact on the metric function $f(r)$, which enters the potential formula.

Next, we analyze the asymptotic behavior of the effective potential $V_{\text{eff}}(r)$ and the corresponding solution $u(r)$ to the radial Eq. (64). As $r \to r_+$, the event horizon, the metric function $f(r) \to 0$, and the effective potential tends to [28]

$$V_{\text{eff}}(r) \to k_+^2 = \left(\omega - \frac{Q}{r_+} \right)^2. \tag{66}$$

In this region, the solution to the wave equation becomes:

$$u_+(r_*) = A_t e^{-ik_+ r_*}, \tag{67}$$

where A_t is a complex amplitude and $k_+ = \omega - Q/r_+$. The physical boundary condition requires that only ingoing waves are present at the event horizon, ensuring causal propagation into the . In this limit, the metric function approaches $f(r) \to 1$ and the effective potential simplifies to [28]

$$V_{\text{eff}}(r) \to k_\infty^2 = \omega^2. \tag{68}$$

Therefore, the asymptotic behavior of the wave function is given by

$$u_\infty(r_*) = A_i e^{-ik_\infty r_*} + A_r e^{ik_\infty r_*}, \tag{69}$$

where A_i and A_r represent the amplitudes of the incoming and reflected waves, respectively, with $k_\infty = \omega$. This asymptotic form underpins the analysis of the superradiance phenomenon, wherein the reflected wave may be amplified ($|A_r| > |A_i|$) as energy is extracted from the BH. The boundary condition in Eq. (69) represents an incoming wave of amplitude A_i arriving from spatial infinity. This wave scatters off the effective potential $V_{\text{eff}}(r)$, resulting in a reflected wave (with amplitude A_r) and a transmitted wave that crosses the horizon (with amplitude A_t), as described by Eq. (67). To examine the scattering process, we evaluate the Wronskian in both the near-horizon and asymptotic regions. In the vicinity of the event horizon, the Wronskian takes the form [28]

$$W_+ = u_+ \frac{du_+^*}{dr_*} - u_+^* \frac{du_+}{dr_*} = 2ik_+ |A_t|^2, \tag{70}$$

where u_+^* is complex conjugate of u_+. Similarly, near spatial infinity, the Wronskian is

$$W_\infty = u_\infty \frac{du_\infty^*}{dr_*} - u_\infty^* \frac{du_\infty}{dr_*} = ik_\infty(|A_i|^2 - |A_r|^2). \tag{71}$$

Equating Eqs. (70) and (71), we obtain the energy conservation relation:

$$|A_i|^2 - |A_r|^2 = \frac{2k_+}{k_\infty}|A_t|^2. \tag{72}$$

For superradiance to take place, the amplitude of the reflected wave must exceed that of the incident wave

$$|A_r|^2 > |A_i|^2 \quad \Rightarrow \quad |A_i|^2 - |A_r|^2 < 0.$$

From Eq. (72), this condition is satisfied if:

$$0 < \omega < \frac{Q}{r_+}. \tag{73}$$

The threshold frequency $\omega_c \equiv \frac{Q}{r_+}$ matches that of the RN BH [29]. Expressed in terms of the field wavelength λ, this condition can be reform as

$$\frac{2\pi}{Q} \leq \frac{\lambda}{r_+}. \tag{74}$$

This implies that for $Q < 1$, we have $\lambda \gg r_+$. For $Q > 2\pi$, the condition $\lambda \sim r_+$ is satisfied. To quantify superradiance, the amplification factor is defined as [28]

$$Z_{\omega l} = \frac{|A_r|^2}{|A_i|^2} - 1. \tag{75}$$

This measures the fractional energy gain (or loss) in the scattered wave. A positive value of $Z_{\omega l}$ corresponds to superradiant amplification. The amplification factor $Z_{\omega l}$ can be computed by numerically integrating the radial wave Eq. (64) with the effective potential from Eq. (65). The tortoise coordinate r_*, defined in Eq. (63), is evaluated from the metric function $f(r)$. After completing the numerical integration, the reflection and incident amplitudes can be determined, and the amplification factor is calculated using Eq. (75).

Figs. 39 to 41 illustrate the amplification factor $Z_{\omega\ell}$ as a function of the scalar field frequency ω for solutions in DPM, highlighting the influence of the dark photon mass $m_{A'}$ and dark gauge coupling g_D, with a comparison to classical Schwarzschild and RN-like BHs. In Fig. 39, increasing $m_{A'}$ leads to a suppression of the peak amplification, indicating that heavier dark photons dampen the superradiant scattering of scalar fields. This behavior is attributed to the stronger exponential suppression of the effective potential, which reduces the efficiency of wave amplification near the event horizon. Fig. 40 shows that as g_D increases, the peak of $Z_{\omega\ell}$ becomes more pronounced and shifts to higher frequencies, reflecting an enhanced interaction between the scalar field and the spacetime mediated by stronger dark gauge coupling. Fig. 41 provides a direct comparison between the amplification factors for dark photon, Schwarzschild, and RN-like BHs. The amplification in the DPM exceeds that of the Schwarzschild case and exhibits distinct frequency-dependent behavior compared to RN-like geometry, demonstrating that the inclusion of dark sector fields introduces qualitatively new superradiant characteristics. The mathematical modeling stems from solving the charged Klein-Gordon equation in the dark photon-modified background and evaluating reflection coefficients in the asymptotic and near-horizon regimes. Physically, these findings suggest that dark photon interactions can significantly alter the energy extraction process from BHs via superradiance, affecting the stability and evolution of BHs in environments where such fields are present. Superradiance in the presence of dark photons can influence the stability of BHs by extracting rotational energy, potentially leading to gaps in the observed BH mass spin distribution if certain dark photon masses are realized. Moreover, the formation of superradiant bound states can act as sources

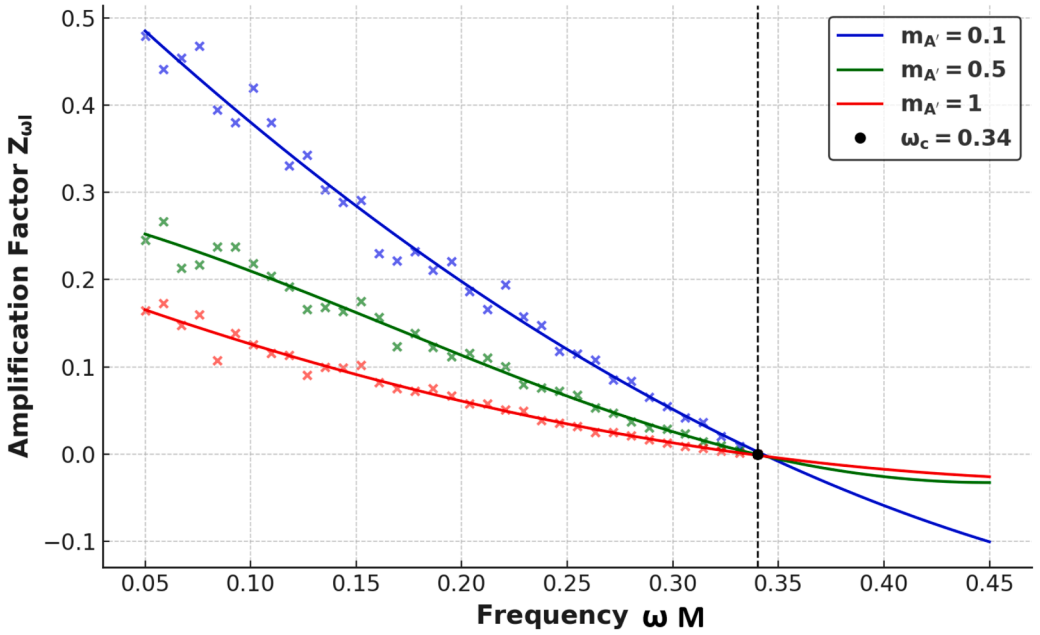

Fig. 39. The plot of amplification factor $Z_{\omega l}$ as a function of frequency ωM for BH solutions in DPM for different values of $m_{A'}M$ for fixed $M = g_D = 0.5$, $\mu_f = S_{12} = 1$ and $\Lambda = 1.7$.

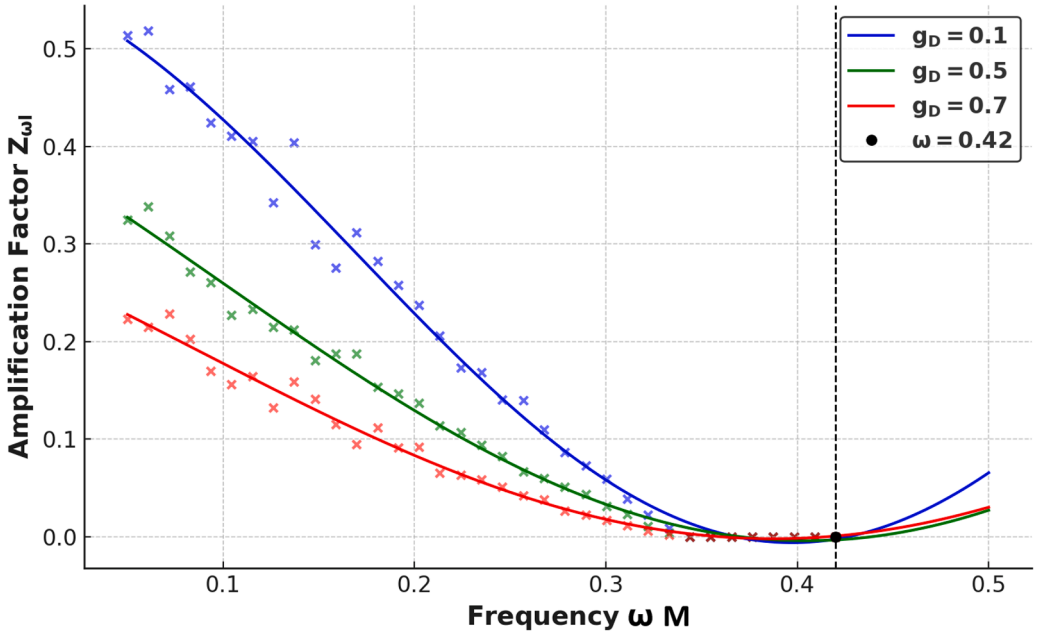

Fig. 40. The plot of amplification factor $Z_{\omega l}$ as a function of frequency ωM for BH solutions in DPM for different values of g_D for fixed $M = m_{A'}M = 0.5$, $\mu_f = S_{12} = 1$ and $\Lambda = 1.7$.

of nearly monochromatic gravitational waves, which could be probed by present and future detectors such as LIGO, LISA, and pulsar timing arrays. Additionally, suppression or enhancement of superradiant modes alters the evolution of accretion disks and jet formation around spinning BHs. Therefore, astrophysical observations of BH spin demographics, continuous-wave gravitational radiation, and jet energetics all provide potential constraints on the parameter space of DPMs.

By incorporating the back-reaction that is, including second-order perturbations of the scalar field on the spacetime geometry and the background vector field, the evolution equations for the BH's mass and charge, resulting from the scattering of a monochromatic

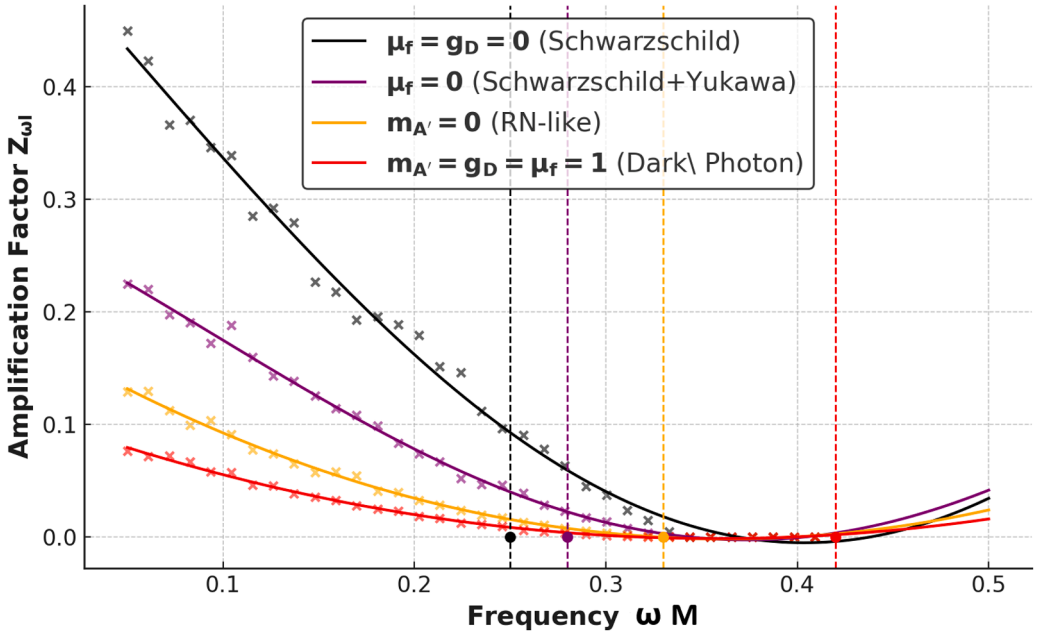

Fig. 41. The plot of amplification factor $Z_{\omega l}$ as a function of frequency ωM for BH solutions in DPM, Schwarzschlid and RN-like BHs.

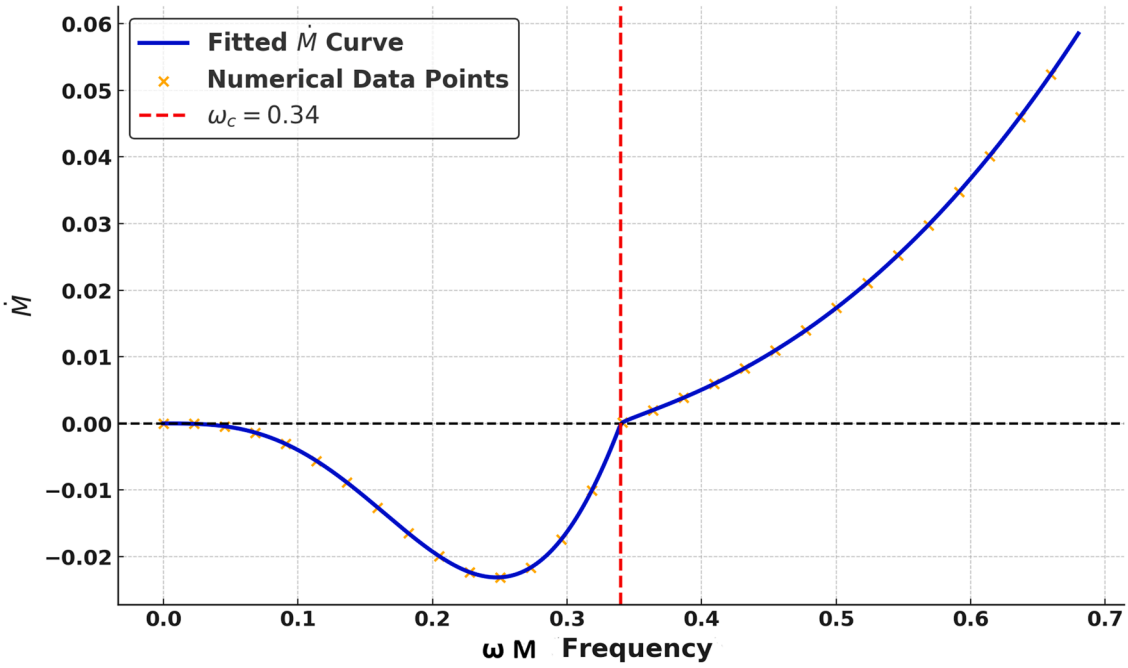

Fig. 42. The plot of mass $\dot{M}$ as a function of frequency ωM for BH solutions in DPM.

wave at large distances which can be derived [27]

$$\dot{M} = -\omega^2\left(|A_r|^2 - |A_i|^2\right), \tag{76}$$

where the dot denotes differentiation with respect to time t, and ω is the frequency of the scalar wave. In the superradiant regime, defined by $\omega < \omega_c$ and $|A_r|^2 - |A_i|^2 > 0$, $\dot{M}$ is negative. This indicates that mass extracted from the and transferred to the exterior region in the form of amplified wave energy. As $\omega \to \omega_c$, the quantity $\dot{M} \to 0$, and the energy flux asymptotically vanishes. In contrast, outside the superradiance regime ($\omega > \omega_c$), $\dot{M}$ is positive, implying that the black hole gains energy and charge from the incident field.

Fig. 42 presents the variation of the mass-loss rate $\dot{M}$ as a function of the scalar field frequency ω for solutions in DPM, offering a direct view into the superradiant energy extraction mechanism. The plot reveals that within the superradiant regime, defined by $\omega < \omega_c = Q/r_+$, the mass-loss rate $\dot{M}$ is negative, indicating that the is losing energy due to the amplification of scattered waves. As ω approaches the critical frequency ω_c, $\dot{M}$ tends toward zero, showing the transition point beyond which superradiance ceases. Outside the superradiant regime ($\omega > \omega_c$), $\dot{M}$ becomes positive, implying that the gains energy from the incident scalar field. This behavior demonstrates consistency with the energy conservation and thermodynamic interpretations of superradiance. The numerical modeling is based on the reflection and transmission coefficients obtained by integrating the radial wave equation derived from the charged Klein-Gordon equation, incorporating the dark photon-modified metric. The shape and magnitude of the $\dot{M}$ curve are sensitive to the parameters $m_{A'}$ and g_D, which govern the form of the effective potential and horizon structure. Physically, this result highlights that dark photon interactions can significantly influence the rate and efficiency of evaporation or growth through superradiant processes. It provides a compelling connection between field-theoretical extensions of gravity and observable evolution, offering a possible avenue for detecting or constraining dark sector properties via the time-dependent behavior of mass in high-energy astrophysical environments.

6. Conclusion

In this work, we have systematically investigated the physical and geometrical properties of BH solutions influenced by dark photon fields, incorporating both Yukawa-type minimal interactions and higher-order magnetic dipole corrections. We explored the gravitational imprint of hidden sector U(1) gauge symmetries specifically dark photons on classical BH metrics. The presence of dark photons not only modifies the spacetime geometry but also introduces nontrivial dynamics through the energy-momentum contributions of dark sector interactions. We began by considering the solution in a spherically symmetric spacetime, modified by effective potentials arising from dark photon interactions. These corrections, embedded in the metric function $f(r)$, depend explicitly on parameters such as the dark photon mass $m_{A'}$, the dark gauge coupling g_D, and the dipole moment scale μ_f/Λ. Our analysis of the horizon structure and thermodynamic quantities revealed that both $m_{A'}$ and g_D significantly influence the event horizon radius and the Hawking temperature, thereby altering the thermal stability and evaporation behavior of the BH in the presence of dark photon corrections.

Moving forward, we examined the geodesic dynamics of massless and massive test particles in the modified spacetime. Through the effective potential formalism, it was shown that the dark photon sector reshapes the photon sphere, modifies the stability of circular orbits, and alters the impact parameter and capture cross-section for light. The analysis of the effective force and Lyapunov exponent further highlighted the role of dark sector parameters in modulating the orbital stability and chaos near the BH. We observed that higher $m_{A'}$ suppresses gravitational attraction at short distances, while larger g_D enhances it, leading to contrasting effects on photon trajectories and matter dynamics. A comprehensive study of the ISCO parameters revealed that dark photon interactions lower the ISCO radius and energy for increasing g_D, while increasing $m_{A'}$ tends to push the ISCO outward. This directly influences accretion disk structure and energy release efficiency. The behavior of angular momentum and orbital velocity profiles further confirmed that these corrections produce measurable deviations in disk rotation curves, suggesting possible constraints from observational astrophysics. The study of the geodetic precession frequency Θ_{GPF} indicated that dark sector fields leave imprints on relativistic frame-dragging, especially near the event horizon.

We also examined the shadow properties of the BH by numerically evaluating the photon sphere radius r_{ph} and the shadow radius R_s. It was demonstrated that increasing $m_{A'}$ compresses the shadow due to exponential suppression, while increasing g_D expands the silhouette by enhancing spacetime curvature. Finally, we investigated the phenomenon of superradiance by solving the Klein-Gordon equation for charged scalar perturbations in the presence of dark photon fields. The conditions for wave amplification were derived, and it was shown that dark sector couplings can significantly enhance or suppress the superradiant scattering process. These findings offer a potential probe into the interaction strength between standard and hidden sectors via astrophysical observables. In conclusion, our study illustrates that the inclusion of dark photon fields in models leads to a wide array of modifications in their thermodynamic, geometric, and dynamical characteristics. These corrections physically manifest as changes in the horizon structure, thermal emission rates, orbital stability, shadow geometry, and wave propagation phenomena.

In comparison to other hidden sector models like scalar fields and axions which often introduce modifications through potential-driven dynamics, leading to phenomena like axion clouds or boson stars, while vector portal models typically couple hidden gauge bosons to the Standard Model via kinetic mixing. The dark photon scenario considered here provides a distinctive mechanism through Yukawa-type interactions and higher-order magnetic dipole corrections, which directly deform the spacetime geometry and strongly affect geodesics, shadows, and superradiance. This comparison highlights the unique feature of the DPM is its ability to simultaneously alter BH optical properties and wave amplification conditions thus offering a complementary and testable pathway relative to other hidden sector candidates. Current instruments such as the Event Horizon Telescope (EHT) already constrain the size and circularity of the M87* and Sgr A* shadows at the $\sim 10\,\%$ level. In our model, variations in the dark photon parameters $(m_{A'}, g_D)$ shift the photon-sphere radius and consequently the shadow size by comparable or larger fractions, depending on the parameter range. This suggests that the present EHT data already provide meaningful constraints on certain regions of the parameter space. Looking forward, next-generation very-long-baseline interferometry (VLBI) arrays, such as the planned EHT, will offer higher dynamic range and angular resolution, allowing for sub-percent level precision in shadow size and potential detection of subtle distortions. Thus, while current EHT observations can place preliminary bounds, future instruments will be able to decisively test the predicted shadow modifications due to dark photons.

Data availability

No data was used for the research described in the article.

Declaration of competing interest

The authors declare that they have no known competing financial interests or personal relationships that could have appeared to influence the work reported in this paper.

Acknowledgment

The authors extend their appreciation to the Deanship of Research and Graduate Studies at King Khalid University for funding this work through Large Research Project under grant number RGP2/381/46

References

[1] M. Fabbrichesi, E. Gabrielli, G. Lanfranchi, The Physics of the Dark Photon: A Primer, Springer Briefs in Physics, 2020. Hep-ph.
[2] J. Redondo, A. Ringwald, Phys. Lett. B 659 (2008) 117.
[3] B. Holdom, Phys. Lett. B 166 (1986) 196.
[4] M. Rogatko, A. Wysokinski, Phys. Rev. B 100 (2019) 84058.
[5] B. Rahmatov et al., Chinese Phys. C 49 (2025) 75105.
[6] R.A. Konoplya, A. Zhidenko, JCAP 12 (2016) 43.
[7] M. Amir, F. Ahmed, S.G. Ghosh, Eur. Phys. J. C 76 (2016) 532.
[8] M. Zahid, et al., Eur. Phys. J. C 82 (2022) 494.
[9] S.U. Islam, R. Kumar, S.G. Ghosh, JCAP 09 (2021) 30.
[10] K. Akiyama, Astrophys. J. Lett 875 (2019) 1.
[11] J. Deng, N. Gao, X. Chen, H. Pu, J. Guo, 278, Ocean Engineering, 2023.
[12] N. Tsukamoto, Z. Li, C. Bambi, JCAP 06 (2014) 43.
[13] S. K. Ullah, et al., Eur. Phys. J. C 84 (2024) 203.
[14] R. Brito, V. Cardoso, P. Pani, 906, Springer, 2015. Gr-qc.
[15] G. Feng, S. Yu, T. Wang, Z. Zhang, Ann. Phys. 473 (2025) 169903.
[16] Y. Wu, Y. Jin, Y. Liu, G. Lyu, Phys. Scripta 100 (2) (2025) 25253.
[17] W.E. East, Phys. Rev. Lett. 121 (2018) 131104.
[18] A.A.A. Filho, K. Jusufi, B. Cuadros-Melgar, G. Leon, A. Jawad, C.E. Pellicer, Phys. Dark Univ. 46 (2024) 101711.
[19] M. Huo, Z. Fan, J. Qi, N. Qi, D. Zhu, J. Guid. Contr. Dyn. 46 (5) (2023) 1015–1022.
[20] A. Ovgn, R.C. Pantig, 2025. Gr-qc.
[21] K. Petraki, L. Pearce, A. Kusenko, JCAP 07 (2014) 39.
[22] A. Al-Badawi, F. Ahmed, I. Sakalli, 2025. Hep-th.
[23] S. Fernando, Gen. Relativ. Gravit. 44 (2012) 1857.
[24] K. Nozari, S. Saghafi, M. Hajebrahimi, K. Jusufi, 2025. Gr-qc.
[25] W. Feng, Z. Fan, J. Qi, M. Huo, N. Qi, IEEE Trans. Aerosp. Electron. Syst. 61 (2) (2025) 2601–2611.
[26] J. Deng, N. Gao, X. Chen, Thin-Walled Structures, 184, 2023.
[27] R. Brito, V. Cardoso, P. Pani, Lect. notes Phys. 906 (2015) 1237.
[28] S.N. Sajadi, S. Ponglertsakul, arXiv:2505, 2025. Gr-qc.
[29] L.C.B. Crispino, S.R. Dolan, E.S. Oliveira, Phys. Rev. D 79 (2009) 64022.